Article

Porphyry copper formation driven by water-fluxed crustal melting during flat-slab subduction

Check for updates

Thomas N. Lamont [1] ✉, Matthew A. Loader[2], Nick M. W. Roberts [3], Frances J. Cooper [1,4], Jamie J. Wilkinson [2,5], Dan Bevan [1,6], Adam Gorecki[7], Anthony Kemp [6], Tim Elliott [1], Nicholas J. Gardiner [8] & Simon Tapster [3]

The prevailing view of the formation of porphyry copper deposits along convergent plate boundaries involves deep crustal differentiation of metal-bearing juvenile magmas derived from the mantle wedge above a subduction zone. However, many major porphyry districts formed during periods of flat-slab subduction when the mantle wedge would have been reduced or absent, leaving the source of the ore-forming magmas unclear. Here we use geochronology and thermobarometry to investigate deep crustal processes during the genesis of the Late Cretaceous–Palaeocene Laramide Porphyry Province in Arizona, which formed during flat-slab subduction of the Farallon Plate beneath North America. We show that the isotopic signatures of Laramide granitic rocks are consistent with a Proterozoic crustal source that was potentially pre-enriched in copper. This source underwent water-fluxed melting between 73 and 60 Ma, coincident with the peak of granitic magmatism (78–50 Ma), porphyry genesis (73–56 Ma) and flat-slab subduction (70–40 Ma). To explain the formation of the Laramide Porphyry Province, we propose that volatiles derived from the leading edge of the Farallon flat slab promoted melting of both mafic and felsic pre-enriched lower crust, without requiring extensive magmatic or metallogenic input from the mantle wedge. Other convergent plate boundaries with flat-slab regimes may undergo a similar mechanism of volatile-mediated lower-crustal melting.

Flat-slab subduction (slab dip < 15°; Fig. 1b) currently occurs at ~10% of convergent plate boundaries[1] and can result from the burial of young, warm, buoyant oceanic lithosphere[1], or when the rate of slab advance is greater than the rate of slab rollback in a fixed mantle reference frame[2]. This geodynamic scenario has been linked to major periods of orogenesis[1,3–5], inland migration and subsequent cessation of arc magmatism[1,4–7], changes in upper-plate thermal structure[3,6], and the formation of some of the largest porphyry copper deposits (PCDs) on Earth (for example, Río Blanco–Los Bronces, and La Escondida, Chile,

and Resolution, Arizona, USA)[7–12]. However, despite the potential importance of flat-slab regimes to supply the copper and associated metals (for example, Au and Mo) required to meet global net-zero emissions goals, their role in ore formation is poorly understood.

Traditional PCD models assume the ore-forming magmas derive from juvenile basaltic melts formed from metasomatism of the mantle wedge above a steeply dipping subducting slab[13–15] (Fig. 1a). Magma differentiation depth proxies (high Sr/Y, La/Yb and (Eu/Eu*)/Yb ratios) suggest PCD formation is favoured in thickened continental crust
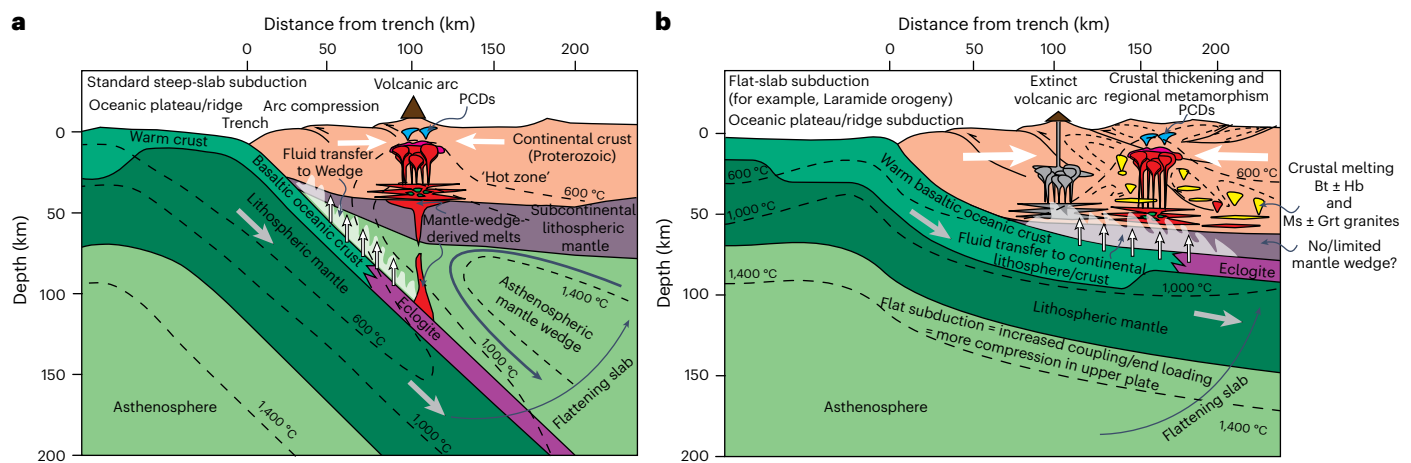
Fig. 1 | Contrasting models for the formation of PCDs along convergent plate boundaries. a, 'Standard' steep-slab subduction with magmatic arc and PCDs sourced from mantle-wedge-derived melts[14]. **b**, Flat-slab subduction analogous to subduction of the Farallon plate during the Laramide orogeny. Here forced flow into the mantle wedge is cut off, and volatiles derived from the slab (H_2O, CO_2, Cl and S) pass straight into the base of the crust, triggering water-fluxed crustal anatexis, granitic magmatism and, potentially, PCD formation. Bt, biotite; Hb, hornblende; Ms, muscovite; Grt, garnet. Data from ref. 14.

within mature compressional arcs[11,12,15], which often correlate with flat-slab regimes[11,12]. Such deeply differentiated magmas are interpreted to contain high concentrations of volatiles (H_2O, CO_2, Cl and S), which are critical in controlling the ultimate enrichment of copper[10–15]. However, during flat-slab subduction, the mantle wedge is reduced, if not absent, meaning that substantial mantle melting cannot occur[1–6,9] (Fig. 1b), and leaving it unclear from where the ore-forming magmas were derived.

The ~80–40 Myr-old Laramide orogeny, western North America[3,4,6], represents a unique opportunity to address this paradox as it was associated with crustal thickening and magmatism that reached >2,000 km inland[3,4,6] and formed the world's second largest PCD province[9,16,17]. The most prominent model to explain the Laramide orogeny involves flat-slab subduction of the Farallon plate[3,4,18–21] in response to the subduction of two oceanic plateaus (Shatsky at ~90 million years ago (Ma) (refs. 19,20) and Hess at ~75–70 Ma (refs. 21,22)) in combination with westward movement of North America[2,19]. An alternative model involves the oblique collision of offshore terranes[22] based on palaeomagnetic evidence that accreted terranes moved thousands of kilometres northwards between ~85 and 55 Ma. In this Article, we integrate geochemical and isotopic data of Laramide granitic rocks with petrological and geochronological constraints from deep crustal exposures, which provide critical insights into the roles of crustal anatexis and flat-slab subduction in the genesis of the Laramide Porphyry Province.

## Laramide flat-slab subduction and crustal anatexis

The Laramide Orogen in Arizona is characterized by (1) contemporaneous biotite ± hornblende-bearing and muscovite ± garnet + magnetite-bearing granitic intrusions spanning ~78–50 Ma (refs. 9,16,23–25); (2) PCDs that formed between ~73 and 56 Ma (refs. 9,16,17,23–26; Supplementary Table 1); and (3) contractional structures active between ~80 and 56 Ma (refs. 23,26–29). All these features are concentrated in a northwest–southeast trending belt along the southern margin of the relatively undeformed Colorado Plateau (the Colorado Plateau Transition Zone, CPTZ; Fig. 2b)[16,17,26]. Within the CPTZ, most PCDs (for example, Ray, Resolution and Morenci; Fig. 2b) are associated with biotite ± hornblende-bearing intrusions[9,16,17] with elevated whole-rock Sr/Y, La/Yb and (Eu/Eu*)/Yb ratios[9,16,17] typical of 'fertile' PCD-related magmas[15] (Supplementary Table 2). These magmas are traditionally described as mantle-derived melts that have had

considerable crustal input[30–32]; however, we question this interpretation for the following reasons.

A compilation of geochronology data across the western United States (Supplementary Table 1) reveals that Laramide volcanism terminated ~2–5 million years before PCD formation, suggesting the ore-forming intrusions developed during a distinct phase of plutonism in a volcanically inactive arc segment following the relaxation of contractional deformation[26–29]. Laramide intrusions are weakly to strongly peraluminous (aluminium saturation index = 1.00–1.15), highly siliceous (SiO_2 > 60–65%) and have low maficity (molar Mg + Fe < 0.1), which overlaps with the compositional range of experimentally derived lower-crustal melts[33] (Extended Data Fig. 1). Furthermore, several prospective PCDs (for example, Diamond Joe and Texas Canyon; Fig. 2b) are associated with muscovite ± garnet-bearing granites, which also display elevated fertility indices (Extended Data Fig. 1 and Supplementary Table 2) and are derived from crustal sources judging from their isotopic signatures[34–37]; this implies that crustal anatexis may be important for regional metallogeny.

Insights into the geodynamic setting and sources of Laramide granitic magmas can be gleaned from whole-rock Sr–Nd–Pb data[30–32] and Hf-in-zircon isotopes[34–37] (Fig. 3). A compilation of igneous rocks younger than 140 Ma across the southwest United States and northwest Mexico (Fig. 3a and Supplementary Table 3) shows (1) decreasing $\varepsilon Nd(t)$ (where $\varepsilon Nd(t)$ represents the εNd value for the rock, calculated at time (t), i.e. the crystallization age) between 110 and 75 Ma, reflecting a progressively diminishing contribution of mantle-wedge-derived magma; (2) negative (that is, unradiogenic) $\varepsilon Nd(t)$ during the Laramide orogeny (75–40 Ma) that overlaps with Proterozoic basement values, consistent with a substantial magma component deriving from such crustal sources; and (3) increasing $\varepsilon Nd(t)$ after 40 Ma, suggesting an increasing contribution of juvenile magma associated with renewed asthenospheric melting following Farallon slab rollback or foundering[38].

In Arizona, Laramide intrusions (~78–50 Ma) fit this isotopic framework, with unradiogenic Nd signatures (biotite ± hornblende-bearing granites: $\varepsilon Nd(t)$ = −0.2 to −13.5; muscovite ± garnet-bearing granites: $\varepsilon Nd(t)$ = −3.0 to −18.4; Fig. 3b–d) and >1 billion years ago (Ga) two-stage Nd and Pb model ages that imply a crustal origin (Fig. 3c and Supplementary Table 3). These data overlap with the known Proterozoic basement ($\varepsilon Nd(70\,Ma)$ = 1.6 to −21.2), particularly the ~1.1 Ga diabase dykes (Fig. 3b), and CPTZ garnet–clinopyroxene xenoliths, which contain copper-bearing sulfides[39]. The origin of these xenoliths is unclear, but
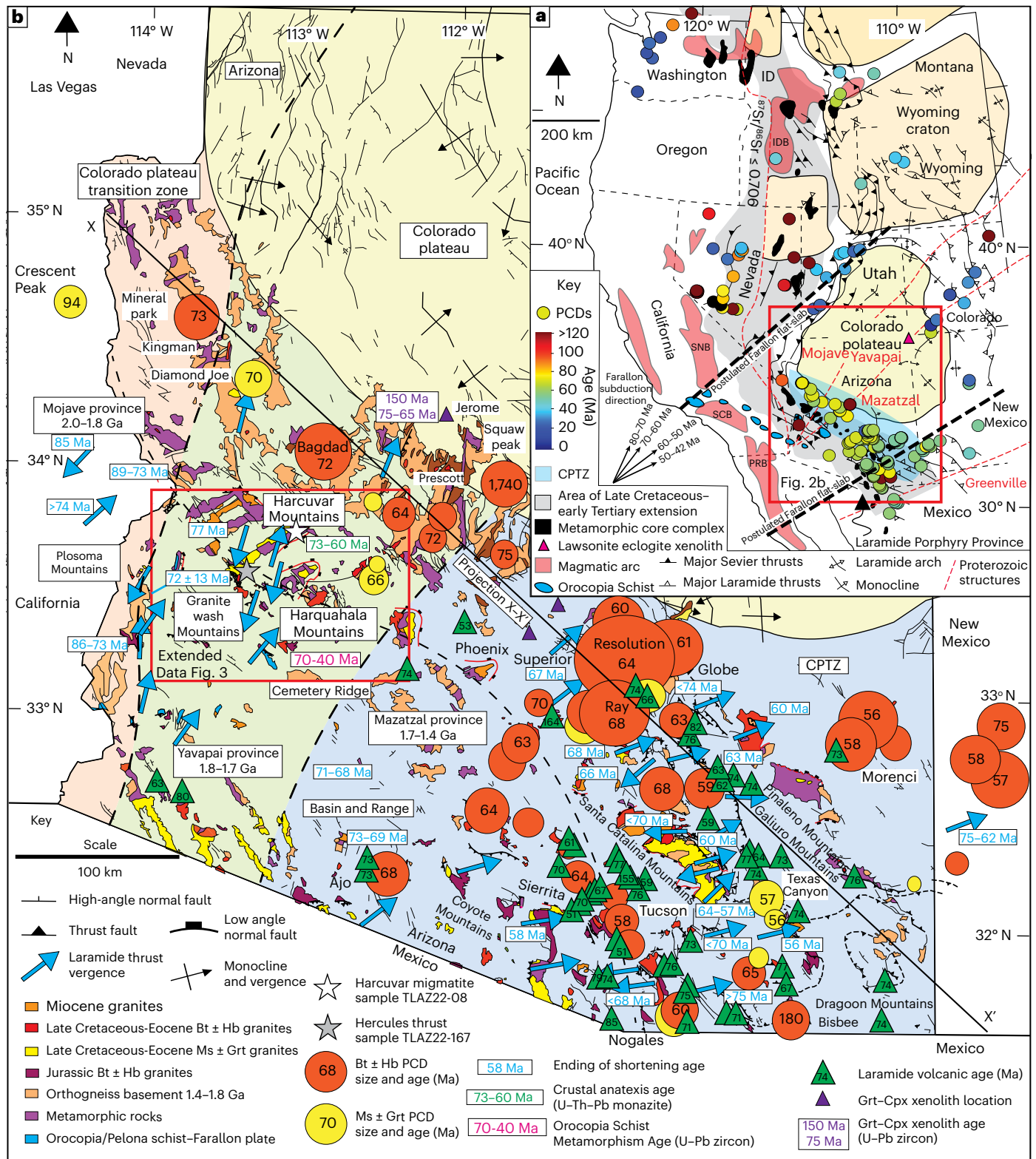
Fig. 2 | Summary maps showing locations and ages of PCDs in the Western USA and Arizona. a, Tectonic setting of PCDs in the western United States. INB, Idaho Batholith; SNB, Sierra Nevada Batholith; SCB, Southern California Batholith; PRB, Peninsular Range Batholith. Data from refs. 3,17,23,26,47,51,52. **b**, Locations of biotite ± hornblende-bearing and muscovite ± garnet-bearing granites, metamorphic rocks, Proterozoic basement granitoids, key structural features (thrust faults, high- and low-angle normal faults and monoclines) and line of projection X–X′ (Fig. 6a). PCDs are represented by circles scaled according to their relative economic value (see Supplementary Table 1 for a compilation of all data). Data from ref. 23. Bt, biotite; Hb, hornblende; Ms, muscovite; Grt, garnet; Cpx, clinopyroxene.

they equilibrated at pressures and temperatures (*P–T*) of 1.0–2.8 GPa and 600–850 °C (ref. 40), at ~150 Ma and ~75 Ma (U–Pb zircon)[38–40] and contain secondary amphibole, indicating they have been subsequently

hydrated. It is possible they are cumulates from juvenile mantle-derived magmas, due to similarity with Sierra Nevada cumulates[39–42]. However, Nd, Pb, Re–Os and Hf-in-zircon mantle extraction ages of
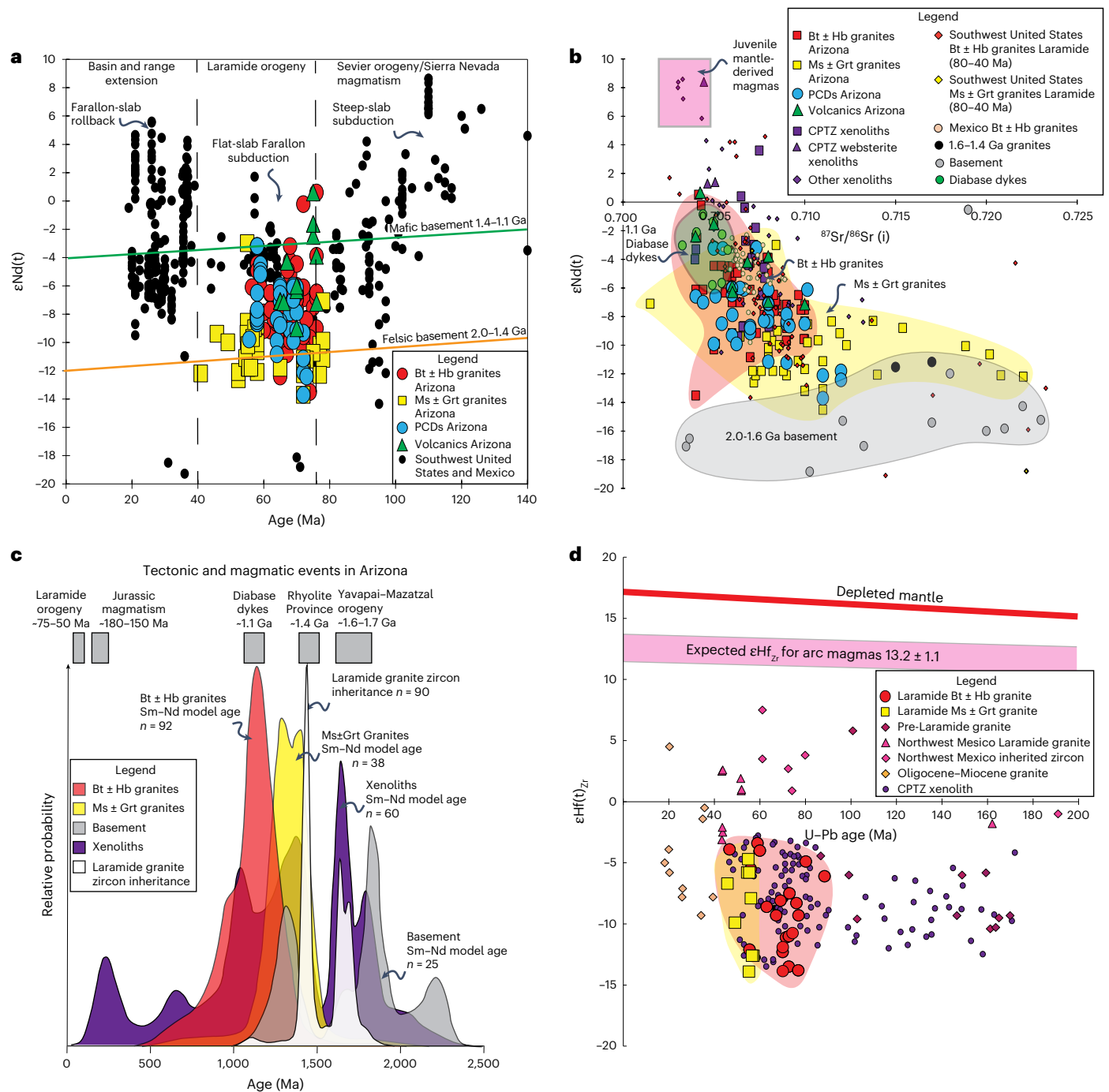
Fig. 3 | A compilation of isotopic data from igneous rocks, xenoliths and basement located in the southwest United States and northwest Mexico. **a**, A compilation of Nd isotopes from igneous rocks formed between 140 Ma and present day highlighting the influence of Farallon flat-slab subduction between ~80 and 40 Ma on magma petrogenesis. Range of calculated basement $\varepsilon Nd(t)$ over this period representing younger (~1.1 Ga) mafic lithologies such as the diabase dykes, garnet–clinopyroxene xenoliths and amphibolites with unradiogenic values representing felsic older (~1.4–2.0 Ga) lithologies, including the Proterozoic granites and Pinal Schist. **b**, Whole-rock Sr–Nd isotopes for biotite ± hornblende and muscovite ± garnet-bearing granites, PCDs, and basement lithologies. Negative $\varepsilon Nd(t)$ suggests all granitoids have unradiogenic

signatures and overlap with the ~1.1 Ga diabase dykes, CPTZ xenoliths and Proterozoic basement. They are notably distinct from the juvenile mantle-wedge-derived magmas. $^{87}Sr/^{86}Sr(i)$ represents the calculated initial $^{87}Sr/^{86}Sr$ ratio for the rock at time of crystallization. **c**, Whole-rock two-stage Sm–Nd model age probability density plot for Laramide biotite ± hornblende-bearing granites, muscovite ± garnet-bearing granites, xenoliths, basement and zircon inheritance. **d**, Hf-in-zircon isotopes from granitic rocks in the southwest United States and northwest Mexico, biotite ± hornblende-bearing granites, muscovite ± garnet-bearing granites, and CPTZ garnet–clinopyroxene xenoliths have overlapping unradiogenic isotopic signatures. Data compiled from sources in Supplementary Table 3.

~2.1–0.5 Ga (refs. 39,43–45) suggest they represent Proterozoic lower crust[43–45] (Fig. 3d). Laramide intrusions also show extensive zircon age inheritance (Fig. 3c), with U–Pb dates of ~1.1, 1.4, 1.6–1.7, 2.0 and 2.6 Ga (refs. 24,46), which overlap with the source crustal residence ages from

Nd isotopes. The younger dates correlate with Yavapai–Mazatzal orogenesis at ~1.7–1.6 Ga (ref. 47), Granite–Rhyolite Province magmatism at ~1.4 Ga and the Southwest Laurentia large igneous province responsible for ~1.1 Ga (ref. 48) diabase dykes.
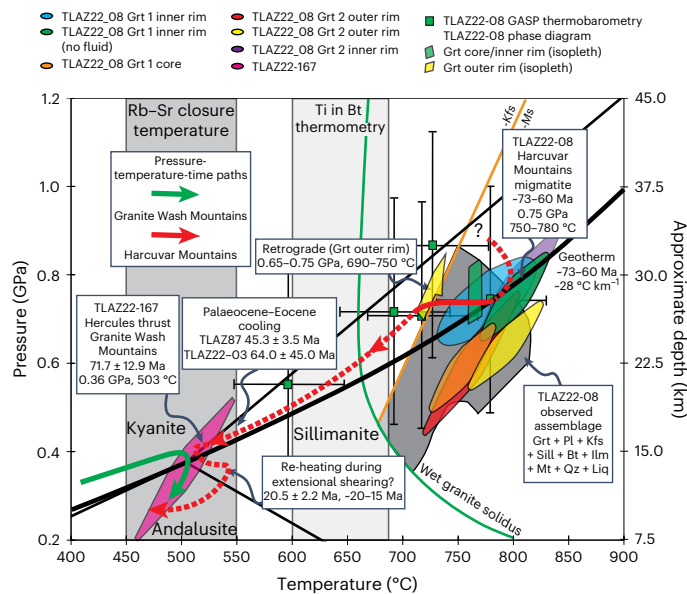
Fig. 4 | Pressure–temperature–time evolution of Laramide-age metamorphic rocks and migmatites from the Harcuvar and Granite Wash mountains in central Arizona. Shaded coloured polygons represent constraints from petrological modelling to 1σ, which considers approximate analytical uncertainties in composition of phases derived from electron probe micro-analysis, bulk-rock composition estimates, and thermodynamic model uncertainties; shaded coloured ellipses represent average P–T calculation results with 2σ uncertainties; and green data points represent garnet–aluminium–silicate–plagioclase and garnet–biotite thermobarometry results with error bars showing 2σ uncertainties. Calculated temperature from titanium-in-biotite thermometry is in the light grey shaded domain, and the estimated 450–550 °C Rb–Sr closure temperature range[65] is in the darker grey domain. U–Th–Pb monazite ages are in red text and Rb–Sr ages in blue text. Observed assemblage for TLAZ22-08 is in the dark grey polygon. Peak metamorphic conditions of 0.75 ± 0.06 GPa and 780 ± 36 °C for sample TLAZ22-08 and 0.36 ± 0.13 GPa and 503 ± 36 °C for sample TLAZ22-167 define a geothermal gradient of ~28 °C km⁻¹ between ~73 and 60 Ma. Garnet outer rim compositions and retrograde biotite constrain cooling of sample TLAZ22-08 from 750 °C to 600 °C at 0.65–0.75 GPa. Pl, plagioclase feldspar; Kfs, potassium feldspar; Ilm, ilmenite; Sill, sillimanite; Qz, quatz; Mt, magnetite; Liq, melt.

Additional constraints can be inferred from exposures of the Oro-copia–Pelona schists at Cemetery Ridge and in the Plomosa Mountains, which are subduction-complex rocks related to the Farallon plate[49–51] (Fig. 2b). Detrital zircon analysis suggests these rocks were deposited at the trench at ~73–70 Ma (refs. 49–51) and underwent prograde metamorphic zircon growth from ~70–65 Ma until ~40 Ma (refs. 49–51) under P–T conditions of 0.8–1.3 GPa and 660 °C. This subduction zone metamorphism temporally and spatially overlaps with the zenith of Laramide magmatism (and PCD formation) and suggests that the leading edge of the Farallon flat slab was transported >500 km directly beneath North America (Fig. 1b). Lawsonite-bearing eclogite xenoliths located ~1,000 km from the trench further indicate that the Farallon flat slab was located at ~120 km depth between ~80 and 30 Ma and removed ~80 km thickness of sub-continental cratonic lithospheric mantle beneath the Colorado Plateau[52,53].

These diverse observations suggest that the mantle wedge beneath the CPTZ was largely eliminated during the genesis of the Laramide Porphyry Province. Isotope mixing calculations (Methods and Extended Data Fig. 2) support this hypothesis, revealing that >70–90% of melt in Laramide granitic magmas was derived from both mafic and felsic Proterozoic crustal sources. From a metallogenic standpoint, ref. 16 suggested that this Proterozoic crust may have sourced the copper in the Arizona PCDs because it contains Proterozoic volcanogenic

massive sulfide deposits (for example, Jerome; Fig. 2b) and the more recently recognized ~1.7 Ga Squaw Peak PCD[54]. Also noteworthy is the higher concentration of PCDs within the Mazatzal Terrane compared with the Yavapai and Mojave Terranes and the abundance of Cu-bearing sulfides in the garnet–clinopyroxene xenoliths, which contain up to ~1,000 ppm Cu (ref. 39).

Critical insights into the timing and conditions of crustal anatexis can be gleaned from exposures of high-grade metamorphic rocks in the Harcuvar, Harquahala and Granite Wash mountains metamorphic core complexes[55–59] (Fig. 2b and Extended Data Fig. 3), which represent the CPTZ mid–lower crust. These rocks provide direct evidence of anatectic processes responsible for the formation of Laramide intrusions and PCDs exposed at higher crustal levels. See Supplementary Tables 4–7 for full results.

Timing and conditions of metamorphism and anatexis

At high structural levels in the Granite Wash Mountains, the Hercules thrust—a major south-southwest-verging Laramide-age contractional structure—preserves syn-kinematic P–T conditions of 0.36 ± 0.13 GPa and 502 ± 36 °C (Fig. 4; TLAZ22-167) in the mylonitized footwall meta-sedimentary rocks, indicating contractional deformation was syn-chronous with regional metamorphism. Metamorphic grade increases with structural depth beneath the Hercules thrust, with exposures of kyanite–sillimanite-bearing schists, migmatites and amphibolites in the Harcuvar Mountains (Figs. 4 and 5). Textures indicate partial melting, including quartzo-feldspathic leucosomes and biotite-rich melanosomes. Leucosomes have diffuse boundaries, trondhjemitic compositions, contain copper and silver oxides, and are complexly folded (Fig. 5c). This suggests that melting occurred during contractional deformation and can be traced from high-melt-fraction domains to garnet–biotite–muscovite leucogranites (for example, Tank Pass and Browns Canyon granites; Extended Data Figs. 3 and 4).

A sample of garnet–sillimanite migmatite (TLAZ22-08) records P–T conditions of 0.75 ± 0.06 GPa and 780 ± 36 °C (~28 km depth; Fig. 4). The lack of primary muscovite is consistent with conditions surpassing muscovite breakdown above the solidus[60,61] (Extended Data Figs. 4–6). However, the low volumetric proportions of peritectic K-feldspar (<3%) and sillimanite (1.8%) relative to leucosome (former melt; 35%) differ from those expected from vapour-absent muscovite dehydration melting[60] (normally in a ratio 8/5/10). This requires anatexis to have occurred with 2.4–3.5 wt% H_2O (Extended Data Figs. 6 and 7), which is considerably greater than the observed mineralogically bound water determined by combining volumetric phase proportions and chemical compositions (1.2 wt% H_2O). Therefore, 1.0–2.2 wt% H_2O was added to the rock during anatexis. Cooling of this sample occurred through conditions of 0.65–0.75 GPa and 600–750 °C (Fig. 4 and Extended Data Fig. 6).

The U–Th–Pb monazite petrochronology suggests anatexis occurred at ~73–60 Ma (Fig. 5 and Extended Data Fig. 8), coincident with migmatite-related leucogranite crystallization at ~78–54 Ma (refs. 56,58,62–64). Older and younger monazite populations record pre-Laramide Sevier orogenesis at ~145 Ma and post-Laramide shearing during Basin and Range extension at ~20–15 Ma. It is also possible that monazite growth and reprecipitation continued from ~60 to 40 Ma, indicated by the younger tail in the ~73–60 Ma population. The Rb–Sr geochronologies of three samples provide overlapping to younger dates of ~72–45 Ma (Extended Data Fig. 9). Given the ~450–550 °C closure temperature[65] of the Rb–Sr system is far below the peak metamorphic temperatures, this suggests that anatexis must have been equivalent to, or older than, these dates. An ~72 Ma date of syn-kinematic mica + plagioclase in the Hercules thrust mylonite constrains the timing of contraction at lower amphibolite-facies conditions. Two further samples yield younger dates of ~26–20 Ma, overlapping with previous thermochronology from the region[66–68],
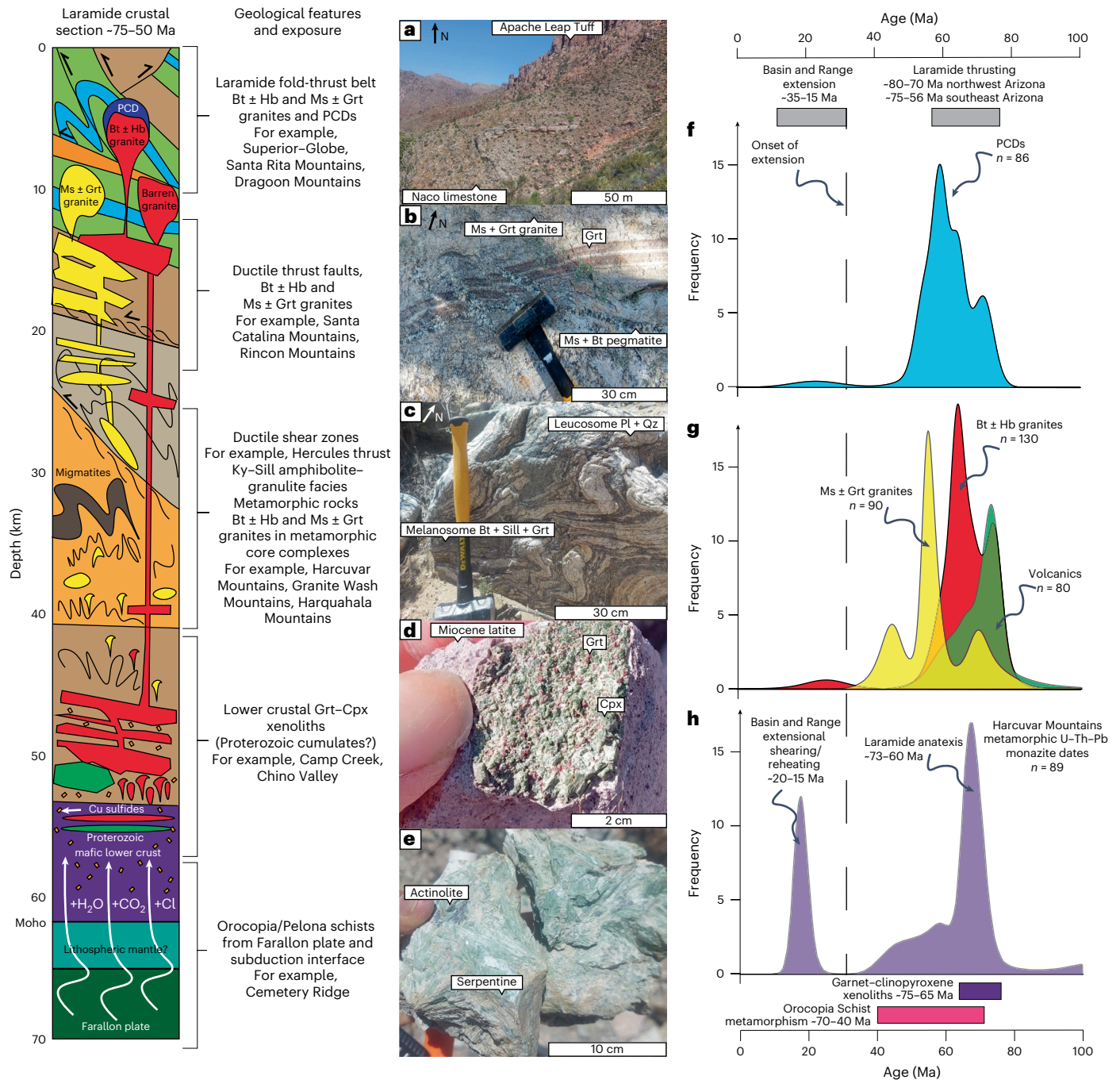
Fig. 5 | Summary of key Laramide geological features in Arizona providing a crustal scale cross-section with corresponding ages, suggesting flat-slab subduction, water-fluxed crustal melting and PCD formation are part of the same process. Left: schematic crustal section of Arizona and corresponding field evidence. **a**, Upper crustal fold-thrust belt and PCDs (for example, Superior/Globe–Miami/San Pedro Valley). **b**, Upper–mid crustal muscovite ± garnet-bearing granites and low-grade metamorphic rocks (for example Santa Catalina Mountains). **c**, Mid–lower crustal high-grade metamorphic rocks and migmatites (for example, Harcuvar and Harquahala mountains) Ky, kyanite; Sill, sillimanite. **d**, Lower-crustal garnet–clinopyroxene xenoliths (for example, Chino Valley). **e**, Accreted pieces of the Farallon slab (Orocopia Schist) and subduction interface of the Farallon plate (for example, minor serpentinized peridotites and Orocopia Schists (mostly pelagic metasediment) at Cemetery Ridge). Right: probability density function plots showing a strong correlation between Laramide orogenesis and anatexis, the zenith of granitic magmatism and porphyry genesis, and metamorphism of the subducted Farallon slab. **f**, Zircon U–Pb and molybdenite Re–Os ages from igneous rocks associated with PCDs (Supplementary Table 1). **g**, U–Pb zircon and K–Ar ages of biotite ± hornblende-bearing and muscovite ± garnet-bearing granites and volcanics (Supplementary Table 1). **h**, Metamorphic U–Th–Pb monazite ages from the Harcuvar Mountains (this study) and U–Pb ages from the Orocopia Schist at Cemetery Ridge, Plomosa Mountains[49–51] and garnet–clinopyroxene xenoliths[39].

suggesting these samples experienced (1) delayed cooling compared with higher structural levels; (2) reheating during Basin and Range extension; and/or (3) isotopic resetting during deformation-induced recrystallization.

Implications for Laramide tectonics

Peak metamorphic conditions of 0.75 GPa and 780 °C at ~73–60 Ma suggest a crustal overburden of ~28 km and an average geothermal gradient of ~28 °C km^{-1} (Fig. 4). The implications are that (1) supra-solidus
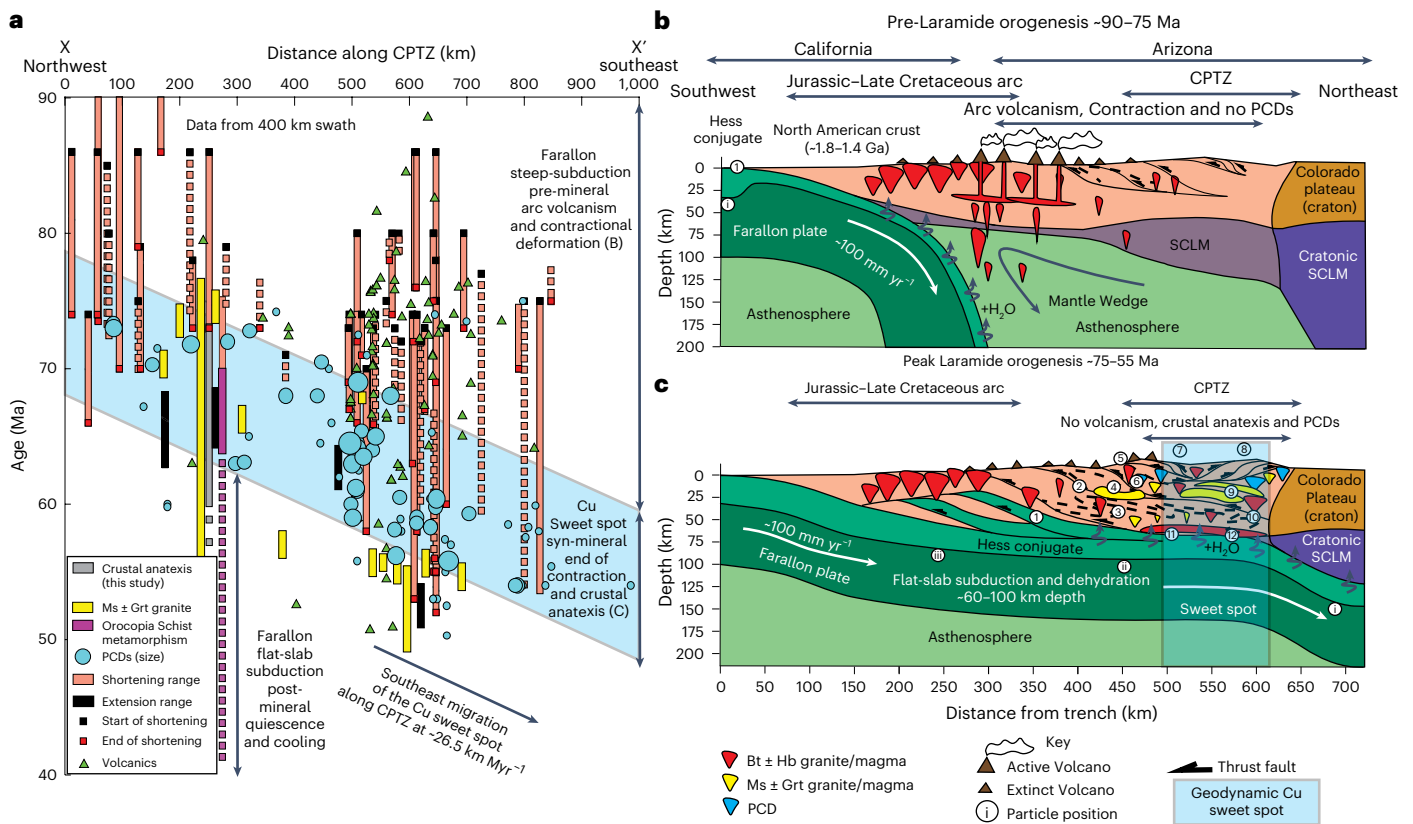
Fig. 6 | Spatial–temporal tectonic–magmatic–mineralization relationships along the CPTZ supporting a flat-slab subduction and crustal anatexis PCD model for Arizona. a, Ages of volcanism, PCDs, shortening and extension, crustal anatexis, Orocopia Schist (ORS) metamorphism and muscovite ± garnet magmatism projected onto a northwest–southeast striking line (X–X′; Fig. 2b) along the CPTZ with a swath of 400 km. Error bars representing 2σ age uncertainties are less than the size of each data point. Dashed bars represent the inferred duration of contractional deformation or metamorphism based on nearby cross-cutting relations and structural constraints (Supplementary Table 1). **b**, Pre-Laramide orogenesis (~90–75 Ma) is associated with steep subduction and arc magmatism/ volcanism in western Arizona and California. **c**, Peak Laramide orogenesis (~75–55 Ma) flat-slab subduction shuts off the mantle wedge, resulting in the termination of arc volcanism and increased end-loading causing crustal thickening and anatexis. Geological features: (1) Orocopia Schist (Farallon Plate) 0.8–1.3 GPa and 660 °C, ~70–65 Ma; (2) Hercules thrust

(top south-southwest), ~85–71 Ma; (3) Harcuvar and Harquahala mountains migmatites 0.75 GPa and 750–780 °C, ~73–60 Ma; (4) Tank Pass and Browns Canyon muscovite ± garnet-bearing granites (cuts Hercules thrust), ~79–70 Ma; (5) northwest Arizona PCDs, ~73–68 Ma (Bagdad, Mineral Park, Diamond Joe, Copper Basin, Crown King); (6) Coyote Mountains Pan-Tak muscovite ± garnet-bearing granite, ~58 Ma, which intruded syn-Baboquivari thrusting (top east-northeast); (7) southeast Arizona PCDs, ~72–56 Ma (for example, Ray, Resolution, Globe–Miami, San Manuel, Copper Creek, Sierra Rita, Texas Canyon, Morenci and Safford); (8) Galiuro Mountains thrusts (top east-northeast), ~73–60 Ma; (9) Santa Catalina Mountains Wilderness and Pinaleño muscovite ± garnet-bearing granites, ~58–50 Ma; (10) 'Maricopa thrust' syn-Wilderness granites (top west-southwest), ~58–50 Ma; (11) water-saturated melting of ~1.7–1.1 Ga mafic lower-crustal source between ~75 and 55 Ma; (12) CPTZ garnet–clinopyroxene xenoliths, ~150 Ma and 75 Ma. Positions (i), (ii) and (iii) represent particle positions on the subducting Farallon slab. SCLM, subcontinental lithospheric mantle.

temperatures occurred at depths >25 km during peak Laramide orogenesis, and (2) the crust reached a minimum thickness of ~50–60 km, based on the addition of the ~28 km overburden to the present-day local Moho depth of ~25–30 km (ref. 69). This thickness is consistent with estimates derived from Sr/Y and La/Yb ratios of Laramide granitic rocks[70] and indicates the crust was thinned by a factor of two during subsequent Basin and Range extension. Notably, our findings argue against the traditional premise that Laramide shortening did not result in considerable crustal thickening in Arizona[26,27].

The timing of water-fluxed crustal anatexis was coincident with the formation of major PCDs (for example, Bagdad at ~72 Ma (ref. 71), Ray at ~72–68 Ma (ref. 24) and Resolution at ~64 Ma (ref. 24); Figs. 2 and 5), the end of contractional deformation (Hercules thrusting at ~72 Ma; Supplementary Table 1) and, most importantly, the onset of flat-slab subduction beneath the CPTZ, evidenced by the isotopic signature of Laramide magmatism (Fig. 3a) and the timing of prograde metamorphism on the Farallon plate (~70–40 Ma (refs. 49–51); Figs. 5 and 6). Integration of these constraints with the potential pre-enrichment of copper in the Proterozoic basement[39,54] supports the hypothesis that

the Laramide Porphyry Province was produced by water-fluxed crustal anatexis during flat-slab subduction.

Along the CPTZ, the timings of contractional deformation (~80–56 Ma), anatexis (~73–60 Ma) and PCD genesis (~73–56 Ma) are also transient at any given location and young towards the southeast at a rate of ~26.5 Myr⁻¹ (Fig. 6a). We propose that all these phenomena are controlled by a common geodynamic mechanism. Flat-slab subduction would cause a diachronous thermal evolution of the North American crust[6,72] due to the interplay between competing mechanisms: (1) increased tractions or end-loading, leading to crustal thickening and heating with characteristic timescales >10 Myr (ref. 73); (2) shear heating along the plate interface (the Moho) given the rapid (~100 mm yr⁻¹ (refs. 18,19)) convergence rate; (3) cooling due to underthrusting of the Farallon plate[6,72]; (4) remnant mantle-wedge heat flow; (5) heat flow from earlier Sevier-related metamorphism (occurring at ~145 Ma). Given these constraints, it is likely that thermal climax and water-fluxed crustal anatexis occurred at a geodynamic 'sweet spot' immediately above the leading edge of the Farallon flat slab as it eroded the cratonic lithosphere (Fig. 6).

At this sweet spot, elevated crustal temperatures would have prevailed due to the proximity to the laterally displaced convecting mantle wedge, in combination with thickened CPTZ crust[5]. Volatiles released from the dehydrating flat slab could also pass across the Moho, facilitating melting of Proterozoic lower crust. This crustal hydration/melting process possibly triggered rheological weakening[74], causing the locus of contractional deformation to migrate further eastwards in front of the leading edge of the flat slab[2,4,5]. However, on timescales >15 Myr, continual underthrusting of the flat slab cooled the North American crust[6,72], as suggested by our ~45–20 Ma Rb–Sr ages. This may explain the systematic spatial-temporal mineralization relationships involving (1) pre-mineralization volcanism, contraction and barren granitic magmatism related to steep subduction that did not sufficiently hydrate the crust, before slab flattening (inboard from the sweet spot), (2) syn-mineralization granitic magmatism and water-fluxed crustal anatexis coinciding with the end of contraction during slab flattening (at the sweet spot), and (3) post-mineralization ore-barren muscovite ± garnet-bearing magmatism, tectonic quiescence and cooling due to continued underthrusting of the Farallon plate after the sweet spot had passed (Fig. 6).

Slab flattening beneath Arizona can be correlated with subduction of the conjugate Hess oceanic plateau at ~75–70 Ma (refs. 19–21) as it can explain prograde metamorphism of the Orocopia–Pelona Schist (~70–65 Ma (refs. 49–51)), water-fluxed anatexis (~73–60 Ma) and the shutdown of arc magmatism in Southern California at ~70 Ma (ref. 21) (Extended Data Fig. 10). Furthermore, if the conjugate Hess was orientated obliquely (north-northeast–south-southwest) with respect to the trench (north-northwest–south-southeast) and convergence vector (northeast), it would intersect the subduction zone at progressively younger times towards the south, causing a diachronous onset of slab flattening and therefore driving the sweet spot southeastwards along the CPTZ (Fig. 6a and Extended Data Fig. 10). Other models including the collision of offshore terranes[22], or subduction of the conjugate Shatsky[18] (which would have been further northeast in Colorado by ~75–70 Ma (refs. 19–21)), have difficulty explaining all these phenomena.

Crustal anatexis drove metallogenesis

We propose that biotite ± hornblende-bearing granitic PCD-related magmas derived from water-fluxed anatexis of mafic (amphibolitic or garnet–pyroxenite) lower-crustal protoliths extracted from the mantle between ~1.7 and 1.1 Ga (Fig. 3c). Dehydration melting is not a plausible mechanism because it is associated with high solidus temperatures and produces low-volume, relatively dry (<2 wt% H_2O)[33,61,75,76] metaluminous magma that is unlikely to form extensive magmatic–hydrothermal systems in the shallow crust. However, we argue that during flat-slab subduction, volatiles migrated across the Moho causing water-fluxed anatexis at depths >25 km. Water-saturated melting of similar mafic lithologies at such depths produces (1) water-rich melt (>8 wt% H_2O)[33,75], (2) larger melt fractions (>50% volume melt)[33,75], (3) peraluminous magma enriched in Na and Al and relatively depleted in Fe, Mg, Ti and K[33,75–77], (4) an increase in amphibole stability as a restitic phase and preferential consumption of plagioclase during anatexis[33,61,75–77], and (5) magma enriched in Sr and depleted in Ba[61]. Such crustal-derived melts would have 'adakite-like' chemistries characterized by elevated Sr/Y, La/Yb and (Eu/Eu*)/Yb ratios[15,33,75–79], as observed in many Laramide intrusions[9,16,17]. Furthermore, we argue that the melt source is equivalent to that of the CPTZ sulfide- and Cu-rich[39] garnet–clinopyroxene xenoliths because these rocks have mantle extraction ages of ~2.1–0.5 Ga (refs. 43–45) and U–Pb zircon dates of ~75 Ma and 150 Ma (refs. 39–41), which overlap with our Laramide and Sevier metamorphic monazite dates (Fig. 5). This implies that metals were recycled from precursor arc cumulates in the lower crust or remnant Proterozoic sub-continental lithosphere[80] due to the addition of water. By contrast, we infer the muscovite ± garnet + magnetite-bearing granites were derived from melting of ~1.7–1.4 Ga granitic basement. Water-fluxed anatexis of this source would form oxidized, volatile-rich and peraluminous magma[60] with elevated fertility indices (Sr/Y and (Eu/Eu*)/Yb)[79] due to consumption of plagioclase during anatexis[61]. Subsequent rollback or foundering of a flat slab can also explain post-orogenic PCDs as this would increase asthenospheric heat flow[38], facilitating melting of the lower crust and sub-continental lithospheric mantle that had been hydrated during previous flat-slab subduction.

We conclude that flat-slab subduction was fundamental to the formation of the Laramide Porphyry Province as it allowed volatiles to flux directly into a lower crust pre-enriched in metals, driving anatexis that led to the formation of ore-forming magmas. It is possible that other convergent plate boundaries with flat-slab regimes underwent a similar mechanism of volatile-mediated lower-crustal anatexis[10]. Our model may explain the correlation between flat-slab subduction and PCD genesis in the southwest United States, central Andes and southeast China, which collectively host >30% of the world's known Cu reserves[17]. We therefore propose flat-slab settings to be favourable exploration targets to meet the ever-increasing global demand for copper.

Online content

Any methods, additional references, Nature Portfolio reporting summaries, source data, extended data, supplementary information, acknowledgements, peer review information; details of author contributions and competing interests; and statements of data and code availability are available at https://doi.org/10.1038/s41561-024-01575-2.

References

1. Gutscher, M. A., Maury, R., Eissen, J. P. & Bourdon, E. Can slab melting be caused by flat subduction? *Geology* **28**, 535–538 (2000).
2. Schepers, G. et al. South-American plate advance and forced Andean trench retreat as drivers for transient flat subduction episodes. *Nat. Commun.* **8**, 15249 (2017).
3. Axen, G. J., van Wijk, J. W. & Currie, C. A. Basal continental mantle lithosphere displaced by flat-slab subduction. *Nat. Geosci.* **11**, 961–964 (2018).
4. Coney, P. J. & Reynolds, S. J. Cordilleran Benioff zones. *Nature* **270**, 403–406 (1977).
5. Copeland, P., Currie, C. A., Lawton, T. F. & Murphy, M. A. Location, location, location: the variable lifespan of the Laramide orogeny. *Geology* **45**, 223–226 (2017).
6. Liu, X., Wagner, L. S., Currie, C. A. & Caddick, M. J. Implications of flat-slab subduction on hydration, slab seismicity, and arc volcanism in the Pampean region of Chile and Argentina. *Geochem. Geophys. Geosyst.* **25**, e2023GC011317 (2024).
7. Kay, S. M. & Mpodozis, C. Central Andean ore deposits linked to evolving shallow subduction systems and thickening crust. *GSA Today* **11**, 4–9 (2001).
8. Skewes, M. A. & Stern, C. R. Genesis of the giant late Miocene to Pliocene copper deposits of central Chile in the context of Andean magmatic and tectonic evolution. *Int. Geol. Rev.* **37**, 893–909 (1995).
9. Barton, M. D. in *The Third Hutton Symposium on the Origin of Granites and Related Rocks* (eds Brown, M. et al.) 261–280 (GSA, 1996).
10. Bissig, T., Clark, A. H., Lee, J. K. & von Quadt, A. Petrogenetic and metallogenetic responses to Miocene slab flattening: new constraints from the El Indio–Pascua Au–Ag–Cu belt, Chile/Argentina. *Miner. Depos.* **38**, 844–862 (2003).
11. Sillitoe, R. H. in *Porphyry and Hydrothermal Copper and Gold Deposits: A Global Perspective* (ed Porter, T. M.) 21–34 (Australian Mineral Foundation, 1998).
12. Cooke, D. R., Hollings, P. & Walshe, J. L. Giant porphyry deposits: characteristics, distribution, and tectonic controls. *Econ. Geol.* **100**, 801–818 (2005).

13. Sillitoe, R. H. A plate tectonic model for the origin of porphyry copper deposits. *Econ. Geol.* **67**, 184–197 (1972).

14. Wilkinson, J. Triggers for the formation of porphyry ore deposits in magmatic arcs. *Nat. Geosci.* **6**, 917–925 (2013).

15. Loucks, R. Deep entrapment of buoyant magmas by orogenic tectonic stress: its role in producing continental crust, adakites, and porphyry copper deposits. *Earth Sci. Rev.* **220**, 103744 (2021).

16. Lowell, J. D. Regional characteristics of porphyry copper deposits of the southwest. *Econ. Geol.* **69**, 601–617 (1974).

17. Leveille, R. A. & Stegen, R. J. in *Geology and Genesis of Major Copper Deposits and Districts of the World: A Tribute to Richard H. Sillitoe* (eds Hedenquist, J. W. et al.) 361–402 (Society of Economic Geologists, 2012).

18. Livaccari, R. F., Burke, K. & Şengör, A. M. C. Was the Laramide orogeny related to subduction of an oceanic plateau? *Nature* **289**, 276–278 (1981).

19. Liu, L. et al. The role of oceanic plateau subduction in the Laramide orogeny. *Nat. Geosci.* **3**, 353–357 (2010).

20. Fletcher, M., Wyman, D. A. & Zahirovic, S. Mantle plumes, triple junctions and transforms: a reinterpretation of Pacific Cretaceous–Tertiary LIPs and the Laramide connection. *Geosci. Front.* **11**, 1133–1144 (2020).

21. Schwartz, J. J. et al. Magmatic surge requires two-stage model for the Laramide orogeny. *Nat. Commun.* **14**, 3841 (2023).

22. Tikoff, B. et al. in *Laurentia: Turning Points in the Evolution of a Continent* (eds Whitmeyer, S. J. et al.) (GSA, 2022).

23. Richard, S. M., Reynolds, S. J., Spencer, J. E. & Pearthree, P. A. *Geologic Map of Arizona* (Arizona Geological Survey, 2000).

24. Seedorff, E. et al. in *Geologic Excursions in Southwestern North America* (ed Pearthree, P. A.) 369–400 (GSA, 2019); https://doi.org/10.1130/2019.0055(15)

25. Greig, R. E. & Barton, M. D. in *Geologic Excursions in Southwestern North America* (ed Pearthree, P. A.) 401–406 (GSA, 2019).

26. Hildenbrand, T. G., Berger, B., Jachens, R. C. & Ludington, S. Regional crustal structures and their relationship to the distribution of ore deposits in the western United States, based on magnetic and gravity data. *Econ. Geol.* **95**, 1583–1603 (2000).

27. Rehrig, W. A. & Heidrick, T. L. in *Tectonic Digest* (eds Wilt, J. C. & Jenney, J. P.) 205–228 (Arizona Geological Survey, 1976).

28. Seedorff, E., Richardson, C. A., Favorito, D. A., Barton, M. D. & Greig, R. E. in *Geologic Excursions in Southwestern North America* (ed. Pearthree, P. A.) 319–335 (GSA, 2019); 10.1130/2019.0055(13)

29. Favorito, D. A. & Seedorff, E. Laramide uplift near the Ray and Resolution porphyry copper deposits, southeastern Arizona: insights into regional shortening style, magnitude of uplift, and implications for exploration. *Econ. Geol.* **115**, 153–175 (2020).

30. Farmer, G. L. & Depaolo, D. J. Origin of Mesozoic and Tertiary granite in the western United States and implications for pre-Mesozoic crustal structure: 2. Nd and Sr isotopic studies of unmineralized and Cu- and Mo-mineralized granite in the Precambrian craton. *J. Geophys. Res.* **89**, 10141–10160 (1984).

31. Lang, J. R. & Titley, S. R. Isotopic and geochemical characteristics of Laramide magmatic systems in Arizona and implications for the genesis of porphyry copper deposits. *Econ. Geol.* **93**, 138–170 (1998).

32. Bouse, R. M., Ruiz, J., Titley, S. R., Tosdal, R. M. & Wooden, J. L. Lead isotope compositions of Late Cretaceous and early Tertiary igneous rocks and sulfide minerals in Arizona: implications for the sources of plutons and metals in porphyry copper deposits. *Econ. Geol.* **94**, 211–244 (1999).

33. Qian, Q. & Hermann, J. Partial melting of lower-crust at 10–15 kbar: constraints on adakite and TTG formation. *Contrib. Mineral. Petrol.* **165**, 1195–1224 (2013).

34. Fornash, K. F., Patchett, P. J., Gehrels, G. E. & Spencer, J. E. Evolution of granitoids in the Catalina metamorphic core complex, southeastern Arizona: U-Pb, Nd, and Hf isotopic constraints. *Contrib. Mineral. Petrol.* **165**, 1295–1310 (2013).

35. Scoggin, S. H., Chapman, J. B., Shields, J. E., Trzinski, A. E. & Ducea, M. N. Early Paleogene magmatism in the Pinaleño Mountains, Arizona: evidence for crustal melting of diverse basement assemblages during the Laramide orogeny. *J. Petrol.* **62**, egab095 (2021).

36. Chapman, J. et al. The North American Cordilleran Anatectic Belt. *Earth Sci. Rev.* **215**, 103576 (2021).

37. Chapman, J. B. et al. Lithospheric architecture and tectonic evolution of the southwestern US Cordillera: constraints from zircon Hf and O isotopic data. *Geol. Soc. Am. Bull.* **130**, 2031–2046 (2018).

38. Humphreys, E. D. Post-Laramide removal of the Farallon slab, western United States. *Geology* **23**, 987–990 (1995).

39. Chen, K. et al. Sulfide-bearing cumulates in deep continental arcs: the missing copper reservoir. *Earth Planet. Sci. Lett.* **531**, 115971 (2020).

40. Rautela, O. et al. In search for the missing arc root of the Southern California batholith: PTt evolution of upper mantle xenoliths of the Colorado Plateau Transition Zone. *Earth Planet. Sci. Lett.* **547**, 116447 (2020).

41. Chapman, A. D., Rautela, O., Shields, J., Ducea, M. N. & Saleeby, J. Fate of the lower lithosphere during shallow-angle subduction: the Laramide example. *GSA Today* **30**, 4–10 (2020).

42. Chapman, A. D. et al. in *Geologic Excursions in Southwestern North America* (ed. Pearthree, P. A.) 209–235 (GSA, 2019).

43. Esperança, S., Carlson, R. W. & Shirey, S. B. Lower-crustal evolution under central Arizona: Sr, Nd and Pb isotopic and geochemical evidence from the mafic xenoliths of Camp Creek. *Earth Planet. Sci. Lett.* **90**, 26–40 (1988).

44. Smith, D., Arculus, R. J., Manchester, J. E. & Tyner, G. N. Garnet–pyroxene–amphibole xenoliths from Chino Valley, Arizona, and implications for continental lithosphere below the Moho. *J. Geophys. Res.* **99**, 683–696 (1994).

45. Esperança, S., Carlson, R. W., Shirey, S. B. & Smith, D. Dating crust–mantle separation: Re–Os isotopic study of mafic xenoliths from central Arizona. *Geology* **25**, 651–654 (1997).

46. Loader, M. A., Wilkinson, J. J. & Armstrong, R. N. The effect of titanite crystallisation on Eu and Ce anomalies in zircon and its implications for the assessment of porphyry Cu deposit fertility. *Earth Planet. Sci. Lett.* **472**, 107–119 (2017).

47. Karlstrom, K. E. & Humphreys, E. D. Persistent influence of Proterozoic accretionary boundaries in the tectonic evolution of southwestern North America: interaction of cratonic grain and mantle modification events. *Rocky Mt. Geol.* **33**, 161–179 (1998).

48. Bright, R. M., Amato, J. M., Denyszyn, S. W. & Ernst, R. E. U–Pb geochronology of 1.1 Ga diabase in the southwestern United States: testing models for the origin of a post-Grenville large igneous province. *Lithosphere* **6**, 135–156 (2014).

49. Jacobson, C. E., Hourigan, J. K., Haxel, G. B. & Grove, M. Extreme latest Cretaceous–Paleogene low-angle subduction: zircon ages from Orocopia Schist at Cemetery Ridge, southwestern Arizona, USA. *Geology* **45**, 951–954 (2017).

50. Seymour, N. M., Strickland, E. D., Singleton, J. S., Stockli, D. F. & Wong, M. S. Laramide subduction and metamorphism of the Orocopia Schist, northern Plomosa Mountains, west-central Arizona: insights from zircon U–Pb geochronology. *Geology* **46**, 847–850 (2018).

51. Haxel, G. B. et al. *Mantle Peridotite and Associated Metasomatic Rocks in the Orocopia Schist Subduction Channel (Latest Cretaceous) at Cemetery Ridge, Southwest Arizona* (Arizona Geological Survey, 2022).

52. Hernández-Uribe, D. & Palin, R. M. Catastrophic shear-removal of subcontinental lithospheric mantle beneath the Colorado Plateau by the subducted Farallon slab. *Sci. Rep.* **9**, 8153 (2019). (2019).

53. Schulze, D. J., Davis, D. W., Helmstaedt, H. & Joy, B. Timing of the Cenozoic "Great Hydration" event beneath the Colorado Plateau: Th–Pb dating of monazite in Navajo volcanic field metamorphic eclogite xenoliths. *Geology* **43**, 727–730 (2015).

54. Sillitoe, R. H., Creaser, R. A., Kern, R. R. & Lenters, M. H. Squaw peak, Arizona: Paleoproterozoic precursor to the Laramide porphyry copper province. *Econ. Geol.* **109**, 1171–1177 (2014).

55. Reynolds, S. J., Richard, S. M., Haxel, G. B., Tosdal, R. M. & Laubach, S. E. in *Metamorphism and Crustal Evolution of the Western United States* (ed. Ernst, W. G.) 465–501 (Prentice Hall, 1988).

56. Bryant, B. & Wooden, J. L. *Geology of the Northern Part of the Harcuvar Complex, West-Central Arizona* (USGS, 2008).

57. Laubach, S. E., Reynolds, S. J., Spencer, J. E. & Marshak, S. Progressive deformation and superposed fabrics related to Cretaceous crustal underthrusting in western Arizona, USA. *J. Struct. Geol.* **11**, 735–749 (1989).

58. Reynolds, S. J., Spencer, J. E., Laubach, S. E., Cunningham, D. & Richard, S.M. *Geologic Map and Sections of the Granite Wash Mountains, West-Central Arizona [Harcuvar 7.5 min]* (Arizona Geological Survey, 1991).

59. Wong, M. S., Singleton, J. S., Seymour, N. M., Gans, P. B. & Wrobel, A. J. Late Cretaceous–early Paleogene extensional ancestry of the Harcuvar and Buckskin–Rawhide metamorphic core complexes, western Arizona. *Tectonics* **42**, e2022TC007656 (2023).

60. Dyck, B., Waters, D. J., St-Onge, M. R. & Searle, M. P. Muscovite dehydration melting: reaction mechanisms, microstructures, and implications for anatexis. *J. Metamorph. Geol.* **38**, 29–52 (2020).

61. Weinberg, R. F. & Hasalová, P. Water-fluxed melting of the continental crust: a review. *Lithos* **212**, 158–188 (2015).

62. Isachen, C. et al. *U–Pb Geochronological Data from Zircons from Eleven Granitic Rocks in Central and Western Arizona* (Arizona Geological Survey, 1999).

63. DeWitt, E. & Reynolds, S. J. Late Cretaceous plutonism and cooling in the Maria fold and thrust belt, west central Arizona. *Geol. Soc. Am. Abstr. Programs* **22**, abstr. 18 (1990).

64. Knapp, J. H. *Mesozoic Thrusting and Tertiary Detachment Faulting in the Moon Mountains, West-Central Arizona* (Arizona Geological Survey, 2018).

65. Oriolo, S. et al. Geochronology of shear zones—a review. *Earth Sci. Rev.* **185**, 665–683 (2018).

66. Prior, M. G., Stockli, D. F. & Singleton, J. S. Miocene slip history of the Eagle Eye detachment fault, Harquahala Mountains metamorphic core complex, west-central Arizona. *Tectonics* **35**, 1913–1934 (2016).

67. Richard, S. M., McWilliams, M. O. & Gans, P. B. *$^{40}Ar/^{39}Ar$ Dates from the Harquahala and Little Harquahala Mountains, West-Central Arizona* (Arizona Geological Survey, 1998).

68. Singleton, J. S., Stockli, D. F., Gans, P. B. & Prior, M. G. Timing, rate, and magnitude of slip on the Buckskin–Rawhide detachment fault, west central Arizona. *Tectonics* **33**, 1596–1615 (2014).

69. Shehata, M. A. & Mizunaga, H. Moho depth and tectonic implications of the western United States: insights from gravity data interpretation. *Geosci. Lett.* **9**, 23 (2022).

70. Chapman, J. B., Greig, R. & Haxel, G. B. Geochemical evidence for an orogenic plateau in the southern US and northern Mexican Cordillera during the Laramide orogeny. *Geology* **48**, 164–168 (2020).

71. Barra, F., Ruiz, J., Mathur, R. & Titley, S. A Re–Os study of sulfide minerals from the Bagdad porphyry Cu–Mo deposit, northern Arizona, USA. *Miner. Depos.* **38**, 585–596 (2003).

72. English, J. M., Johnston, S. T. & Wang, K. Thermal modelling of the Laramide orogeny: testing the flat-slab subduction hypothesis. *Earth Planet. Sci. Lett.* **214**, 619–632 (2003).

73. England, P. C. & Thompson, A. B. Pressure–temperature–time paths of regional metamorphism I. Heat transfer during the evolution of regions of thickened continental crust. *J. Petrol.* **25**, 894–928 (1984).

74. Humphreys, E. et al. How Laramide-age hydration of North American lithosphere by the Farallon slab controlled subsequent activity in the western United States. *Int. Geol. Rev.* **45**, 575–595 (2003).

75. Beard, J. E. & Lofgren, G. E. Dehydration melting and water-saturated melting of basaltic and andesitic greenstones and amphibolites at 1, 3, and 6.9kb. *J. Petrol.* **32**, 365–401 (1991).

76. Collins, W. J., Murphy, J. B., Johnson, T. E. & Huang, H. Q. Critical role of water in the formation of continental crust. *Nat. Geosci.* **13**, 331–338 (2020).

77. Zhang, J., Chang, J., Wang, R. & Audétat, A. Can post-subduction porphyry Cu magmas form by partial melting of typical lower-crustal amphibole-rich cumulates? Petrographic and experimental constraints from samples of the Kohistan and Gangdese arc roots. *J. Petrol.* **63**, egac101 (2022).

78. Wang, X. et al. Adakite generation as a result of fluid-fluxed melting at normal lower-crustal pressures. *Earth Planet. Sci. Lett.* **594**, 117744 (2022).

79. Yakymchuk, C., Holder, R. M., Kendrick, J. & Moyen, J. F. Europium anomalies in zircon: a signal of crustal depth? *Earth Planet. Sci. Lett.* **622**, 118405 (2023).

80. Pettke, T., Oberli, F. & Heinrich, C. A. The magma and metal source of giant porphyry-type ore deposits, based on lead isotope microanalysis of individual fluid inclusions. *Earth Planet. Sci. Lett.* **296**, 267–277 (2010).

Publisher's note Springer Nature remains neutral with regard to jurisdictional claims in published maps and institutional affiliations.

[1]School of Earth Sciences, University of Bristol, Bristol, UK. [2]London Centre for Ore Deposits and Exploration (LODE), Natural History Museum, London, UK. [3]Geochronology and Tracers Facility, British Geological Survey, Nottingham, UK. [4]Department of Earth Sciences, University College London, London, UK. [5]Department of Earth Science and Engineering, Imperial College London, London, UK. [6]Centre for Exploration Targeting, School of Earth Sciences, University of Western Australia, Perth, Western Australia, Australia. [7]BHP, Tucson, AZ, USA. [8]School of Earth and Environmental Sciences, University of St Andrews, St Andrews, UK. ✉e-mail: thomas.lamont@unlv.edu

Methods

Electron probe micro-analysis

The compositions of phases in samples TLAZ22-08 and TLAZ22-167 were derived from electron probe micro-analysis (EPMA) performed on a CAMECA SX100 electron microprobe in the School of Earth Sciences, University of Bristol. Operating conditions involved an accelerating voltage of 15.0 keV corresponding to a current of 20 nA, a range of primary standards were used, including andradite (Fe, Mg, Ca), TiO_2 (Ti), Mn metal (Mn), labradorite (Na, Al, Si) and sanidine (K) for major elements, and secondary standards include diopside, KK1, SPH Labradorite, RN18 and FDLA1. Garnet line profiles were collected using a 75 µm step size across all garnets from sample TLAZ22-08 corresponding to between 25 and 30 analyses per porphyroblast. Garnets show minor zoning in major elements, with homogeneous cores and resorbed rims (Extended Data Fig. 5 and Supplementary Information). Pyrope [XMg] displays a flat profile across the garnet core and mantle, but then shows convex downtrends (0.18–0.13) from the inner to the outer rim, grossular [XCa] remains either homogeneous or increases slightly from the core towards the outer rim (0.05–0.07), whereas almandine [XFe] remains homogeneous before decreasing towards the outer rim (0.73–0.71). However, spessartine [XMn] is homogeneous or concaves upwards (0.05–0.08) from core to outer rim, indicative of garnet resorption. It is also possible that the increase in grossular and decrease in pyrope at the rim is due to diffusion because of resorption of garnet by biotite. These garnet profiles suggest garnet growth zoning has been modified by diffusion[81], and therefore only peak metamorphic conditions are preserved in the garnet core and inner rim, whereas garnet outer rims record retrograde net transfer reactions[82]. Mineral abbreviations follow the guidelines of ref. 83. Anhydrous phase compositions were calculated to standard numbers of oxygen per formula unit[84], micas were recalculated to 11 oxygens, and chlorite to 28 oxygens. Where present, H_2O content was assumed to occur in stoichiometric amounts. The proportion of Fe^{3+}/Fe_{total} was calculated using AX[85]. The complete EPMA database is presented in Supplementary Table 4.

Thermobarometry and petrological modelling

Several thermobarometric approaches were employed to constrain the $P–T$ conditions of metamorphism, including the Ti-in-biotite thermometer[86], the garnet–biotite thermometer[87], the garnet–aluminosilicate–plagioclase–quartz barometer[85,86], the garnet–muscovite–plagioclase barometer, and average $P–T$ (ref. 88) using THERMOCALC version TC-3.50i with characteristic end members judged to be in textural equilibrium for each sample. The complete results are presented in Supplementary Table 5.

Phase diagram construction was performed using THERMOCALC version TC-350i[89] and Theriak Domino[90] and the internally consistent thermodynamic dataset ds62[91]. Migmatite sample TLAZ22-08 was modelled in the 11-component system $MnO–Na_2O–CaO–K_2O–FeO–MgO–Al_2O_3–SiO_2–H_2O–TiO_2–O$. The $a–x$ relations for solid–solution phases were used: clinopyroxene (diopside–omphacite–jadeite) and clinoamphibole (glaucophane–actinolite–hornblende)[92]; garnet, biotite, muscovite–paragonite, and chlorite, epidote, ilmenite[93]; plagioclase feldspar[94] and melt[95]. Pure phases comprised talc, lawsonite, kyanite, sillimanite, andalusite, zoisite, quartz, coesite and rutile. The effective bulk compositions for sample TLAZ22-08 were calculated using mineral proportions derived by point counted analyses of an entire thin section using J-MicroVision and representative EPMA-derived phase compositions following the method of ref. 96. Details on the determination of the bulk-rock composition used to perform phase equilibrium modelling are shown in the Supplementary Information. Uncertainties related to the absolute positions of assemblage field boundaries calculated phase diagrams have been shown to be less than ±0.1 GPa and ±50 °C at the 2σ (95% confidence) level[87,95], with this variation being largely a function of propagated uncertainty on endmember thermodynamic properties within the dataset. However, because phase diagrams were calculated using the same dataset and $a–x$ relations, it has also been shown that similar absolute errors associated with dataset endmembers cancel, and calculated phase equilibria are relatively accurate to within ±0.02 GPa and ±10–15 °C (refs. 91,97).

The $P–T$ conditions of peak metamorphism were determined by investigating compositional isopleths for pyrope and grossular content in garnet. Since these isopleths vary to first order with changes in pressure and temperature and commonly intersect at high angles, they specify unique intersection points with a high degree of confidence for tracking garnet composition evolution in $P–T$ space. The intersections of isopleths representing measured compositions are represented by shaded polygons indicating uncertainties at the 1σ level calculated by THERMOCALC/Theriak Domino. The results were verified by comparing mineral volumetrically determined mineral proportions by point counting using J-MicroVision and intersection of garnet compositional isopleths with those predicted by the petrological model. The results are in good agreement with conventional thermobarometry. In melting calculations, the bulk-rock supra-solidus water content of sample TLAZ22-08 was varied. In a closed system scenario, the bulk-rock supra-solidus water content was fixed to allow minimal water saturation at the wet solidus, here defined as ~1 mol% free H_2O. It was determined 7 mol% H_2O represents fluid saturation at the wet solidus. Bulk-rock H_2O content was estimated at 4.5 mol% (1.2 wt%), determined by combining point counted volume estimates of hydrous phases and average phase compositions determined by EPMA (Supplementary Information). Temperature–$X(H_2O)$ calculations were performed to test the effect of an open system to simulate water-fluxed melting (Extended Data Figs. 6 and 7 and Supplementary Information).

To investigate the effect of water-fluxed melting, bulk-rock H_2O content was varied between 0.25 wt% H_2O and 6 wt% H_2O at 0.75 GPa. An H_2O content of <1.2 wt% represents a closed system with water derived from hydrous phases in the rocks such as biotite and muscovite, whereas >1.2 wt% H_2O represents an open system and fluxing water from an external source. Phase diagrams demonstrate that above the water-saturated solidus, the addition of water does not drastically change the muscovite dehydration melting reaction, and therefore at peak conditions, anatexis progressed by incongruent breakdown of muscovite and plagioclase. Intersection of mineral volume isopleths was used to constrain the likely range of water contents during melting, and the loss of k-feldspar from the predicted assemblage defines the maximum possible amount of water during which anatexis occurred. It was determined that the observed assemblage equilibrated at supra-solidus conditions with a bulk-rock water content of ~3.0–3.2 wt% H_2O. The predicted major element melt compositions, aluminium saturation index, volumes of restitic phases, melt and magmatic water content are presented in Extended Data Fig. 7 and plotted compared with average Laramide granites. This was calculated using an in-house Matlab script that utilizes the pixelmap output function of Theriak Domino. The full results are presented in the Supplementary Information and Supplementary Table 5 and discussed in the main text.

Sr–Nd isotopes and Sm–Nd model ages

The $^{87}Sr/^{86}Sr$ and $^{143}Nd/^{144}Nd$ measurements were compiled from the literature for Arizona Laramide biotite ± hornblende and muscovite ± garnet-bearing granitoids, PCDs, Laramide volcanics, xenoliths and basement. Initial Sr and Nd isotope ratios were calculated using the available U–Pb magmatic ages or K–Ar ages and decay constants of 1.393×10^{-11} for ^{87}Sr (ref. 98) and 6.524×10^{-12} for ^{147}Sm (ref. 99). Initial Sr isotope values are quoted as $^{87}Sr/^{86}Sr_{(i)}$ and Nd isotope values are quoted as $\varepsilon Nd_{(t)}$ using the CHUR values of ref. 100. Two-stage Nd model ages were calculated using $^{147}Sm/^{144}Nd$ of 0.09 and 0.12, that of average-evolved and less-evolved continental crust[101], respectively, and a depleted mantle with a modern-day $^{143}Nd/^{144}Nd$ of 0.51315 and $^{147}Sm/^{144}Nd$ of 0.2135[102]. Two-component Sr–Nd mixing calculations

were performed between a depleted mantle source and a nominal crustal source. The latter was varied to reflect a mixture of crustal rocks by using the average felsic crust and mafic crust from Arizona. A spectrum of 20 different crustal combinations was used, representing 5% sequential additions of mafic and felsic crust. The resultant calculated mixtures between depleted mantle and 'mixed' crust that were deemed successful plotted within the 95% confidence ellipse for the biotite ± hornblende-bearing granites (Extended Data Fig. 2), and the successful results were plotted as a cumulative density plot to show the statistical likelihood of the relative importance of crustal and mantle sources. The results are compiled with source references in Supplementary Table 3 and the Supplementary Information and strongly suggest that the PCD data can be explained by various combinations of different (crustal) source components. Although we cannot entirely rule out a juvenile mantle-derived component in the formation of the Laramide intrusions, it is likely this component is relatively small.

Rb–Sr geochronology

The analytical procedure for in situ Rb–Sr dating is extremely similar to that described in ref. 103. Samples were analysed using a 193 nm Photon Machines excimer laser equipped with ARIS[103] (aerosol rapid introduction system). Laser operating conditions, which were standardized for dating, were a 110 µm laser spot diameter, which was ablated using a repetition rate of 10 Hz, and a fluence of 7 J cm^{-2} for 600 laser pulses. These spots were positioned to target identified phases of interest, which include feldspar and mica that were exposed on polished surfaces of cut billets. This laser ablation system was coupled with Proteus, a collision-cell multicollector inductively coupled plasma tandem mass spectrometer housed at the University of Bristol. To provide chemical resolution of Rb^+ and Sr^+ during analysis[104], a reaction gas mixture consisting of 5% SF_6 (99.99% purity) in He (99.9999%) was used. The flow rates for the He and SF_6 collision-cell gases were 2 ml min^{-1} and 0.025 ml min^{-1}, respectively. During analysis, the SrF isotopologues ($^{86}SrF^+$, $^{87}SrF^+$ and $^{88}SrF^+$) and atomic $^{85}Rb^+$ and $^{88}Sr^+$ were collected for each spot. The measurement of fluorinated and monoatomic ion species was achieved by adjusting the centre mass of the sector magnetic field of Proteus during analysis. The position of the Faraday cup collectors, integration and idle times were identical to those specified in ref. 103. However, in this method, 10^{13} Ω resistors were used in the collection of $^{87}SrF^+$ and $^{86}SrF^+$ ions to improve signal/noise ratio during collection, and thus improve $^{87}SrF/^{86}SrF$ precision for small ion beam sizes[105–108]. The remaining isotopes, $^{88}SrF^+$, $^{88}Sr^+$ and $^{85}Rb^+$, were collected in Faraday cups that were matched with 10^{11} Ω resistors. To correct for the slower response time of the 10^{13} Ω resistors, relative to 10^{11} Ω resistors, a conventional tau correction method was used[106]. Mean radiogenic Sr isotope ratio $^{87}Sr/^{86}Sr$ for each spot analysis was calculated using the measured $^{87}SrF^+/^{86}SrF^+$ and $^{88}SrF^+/^{86}SrF^+$ to correct for natural and instrumental mass-dependent fractionation by use of an exponential law correction. Residual inaccuracy after the exponential law correction was externally normalized using well-characterized in-house feldspar standard Te-1[103], which was analysed every ~10 sample analyses. Sample analyses that were beyond the mean $^{88}SrF^+/^{86}SrF^+$ ratio ±2σ uncertainty measured for Te-1 were excluded due to the presence of an isobaric interference on $^{86}SrF^+$.

Mean sample $^{87}Rb/^{86}Sr$ ratios for each spot analysis were converted using measured $^{85}Rb^+/^{88}SrF^+$ ratios, which were externally normalized to analysis of NIST SRM 610 glass and a $^{87}Rb/^{86}Sr$ ratio of 2.389 (ref. 103). Correlation coefficients were also calculated for measured $^{85}Rb^+/^{88}SrF^+$ and $^{87}SrF^+/^{86}SrF^+$ ratios. Differential Rb–Sr elemental fractionation of the NIST SRM 610 glass standard and sample minerals was corrected for the analytical session using the Dartmoor granite (DG-1) as a secondary standard[109]. An $^{87}Rb/^{86}Sr$ correction factor of 0.952 ± 0.011 was determined from the analysis of plagioclase feldspar, K-feldspar and biotite in DG-1. This single correction factor was applied to all calculated sample feldspar and mica $^{87}Rb/^{86}Sr$ ratios in this study.

The Rb–Sr ages, initial radiogenic Sr isotope ratios and uncertainties were all calculated using the open access software package IsoplotR[110] using input mean calculated $^{87}Rb/^{86}Sr$, $^{87}Sr/^{86}Sr$ ratios with associated 2σ uncertainties and correlation coefficient values. Total age uncertainties were then calculated by accounting for the relative uncertainty of sample isochron slope calculated in IsoplotR[110] and the relative uncertainty of the DG-1 isochron slope used for calculation of the $^{87}Rb/^{86}Sr$ correction factor[104]. The full results are presented in Supplementary Table 6.

U–Th–Pb geochronology

In situ laser ablation inductively coupled plasma mass spectrometry (ICP-MS) U–Th–Pb split-stream geochronology was conducted at the Geochronology and Tracers Facility, British Geological Survey. The U–Th–Pb measurements were collected on a Nu Instruments Attom single-collector ICP-MS following similar analytical conditions and measurement protocols to those described previously[111], with detailed methodology provided in the Supplementary Information. Laser conditions were a 14 µm spot size, 10 Hz repetition rate, 17 s of ablation using a fluence of 3.1 J cm^{-2}. The He carrier gas was split after exiting the laser and sent to both the single-cell ICP-MS for U–Th–Pb and an Agilent 7500 quadrupole ICP-MS for measurement of trace elements. The full analytical conditions for both instruments are provided in Supplementary Table 7. Matrix-matched normalization using standard sample bracketing was used for U–Th–Pb geochronology and trace elements, with data reduction for geochronology comprising the Attolab TRA software and in-house spreadsheet, and Iolite4[112] for trace elements. Monazites 44069[113] and Bananeira[114] were used as primary reference materials for normalization of U–Th–Pb and trace elements, respectively. Internal standardization of trace elements used ^{31}P assuming 22.45 wt%. All plotting and age calculations were conducted with IsoplotR[110] and are shown and quoted at 2σ.

Data availability

Code availability

References

81. Caddick, M. J., Konopásek, J. & Thompson, A. B. Preservation of garnet growth zoning and the duration of prograde metamorphism. *J. Petrol.* **51**, 2327–2347 (2010).

82. Kohn, M. J. & Spear, F. S. Retrograde net transfer reaction insurance for pressure–temperature estimates. *Geology* **28**, 1127–1130 (2000).

83. Whitney, D. L. & Evans, B. W. Abbreviations for names of rock-forming minerals. *Am. Mineral.* **95**, 185–187 (2010).

84. Howie, R. A., Zussman, J. & Deer, W. *An Introduction to the Rock-Forming Minerals* (Longman, 1992).

85. Holland, T. J. AX: a program to calculate activities of mineral end-members from chemical analyses (Univ. Cambridge, 2009); https://filedn.com/lU1GlyFhv3UuXg5E9dbnWFF/TJBHpages/ax.html

86. Henry, D. J., Guidotti, C. V. & Thomson, J. A. The Ti-saturation surface for low-to-medium pressure metapelitic biotite: implications for geothermometry and Ti-substitution mechanisms. *Am. Mineral.* **90**, 316–328 (2005).

87. Spear, F. S. *Metamorphic Phase Equilibria and Pressure-Temperature-Time Paths* (Mineralogical Society of America, 1993).

88. Bhattacharya, L., Mohanty, L., Maji, A., Sen, S. K. & Raith, M. Non-ideal mixing in the phlogopite-annite binary: constraints from experimental data on Mg–Fe partitioning and a reformulation of the biotite–garnet geothermometer. *Contrib. Mineral. Petrol.* **111**, 87–93 (1992).

89. Powell, R. & Holland, T. J. On thermobarometry. *J. Metamorph. Geol.* **26**, 155–179 (2008).

90. de Capitani, C. & Petrakakis, K. The computation of equilibrium assemblage diagrams with Theriak/Domino software. *Am. Mineral.* **95**, 1006–1016 (2010).

91. Holland, T. J. B. & Powell, R. An improved and extended internally consistent thermodynamic dataset for phases of petrological interest, involving a new equation of state for solids. *J. Metamorph. Geol.* **29**, 333–383 (2011).

92. Green, E. C. R. et al. Activity–composition relations for the calculation of partial melting equilibria in metabasic rocks. *J. Metamorph. Geol.* **34**, 845–869 (2016).

93. White, R. W., Powell, R., Holland, T. J. B., Johnson, T. E. & Green, E. C. R. New mineral activity–composition relations for thermodynamic calculations in metapelitic systems. *J. Metamorph. Geol.* **32**, 261–286 (2014).

94. Holland, T. J. B., Green, E. C. R. & Powell, R. A thermodynamic model for feldspars in $KAlSi_3O_8$–$NaAlSi_3O_8$–$CaAl_2Si_2O_8$ for mineral equilibrium calculations. *J. Metamorph. Geol.* **40**, 587–600 (2022).

95. Holland, T. J. B., Green, E. C. R. & Powell, R. Melting of peridotites through to granites: a simple thermodynamic model in the system KNCFMASHTOCr. *J. Petrol.* **59**, 881–900 (2018).

96. Carson, C. J., Powell, R. & Clarke, G. Calculated mineral equilibria for eclogites in CaO–Na2O–FeO–MgO–Al2O3–SiO2–H2O: application to the Pouebo Terrane, Pam Peninsula, New Caledonia. *J. Metamorph. Geol.* **17**, 9–24 (1999).

97. Palin, R. M., Weller, O. M., Waters, D. J. & Dyck, B. Quantifying geological uncertainty in metamorphic phase equilibria modelling; a Monte Carlo assessment and implications for tectonic interpretations. *Geosci. Front.* **7**, 591–607 (2016).

98. Nebel, O., Scherer, E. E. & Mezger, K. Evaluation of the ^{87}Rb decay constant by age comparison against the U–Pb system. *Earth Planet. Sci. Lett.* **301**, 1–8 (2011).

99. Villa, I. M. et al. IUPAC-IUGS recommendation on the half-lives of ^{147}Sm and ^{146}Sm. *Geochim. Cosmochim. Acta* **285**, 70–77 (2020).

100. Bouvier, A., Vervoort, J. D. & Patchett, P. J. The Lu–Hf and Sm–Nd isotopic composition of CHUR: constraints from unequilibrated chondrites and implications for the bulk composition of terrestrial planets. *Earth Planet. Sci. Lett.* **273**, 48–57 (2008).

101. Taylor, S. R. & McLennan, S. M. *The Continental Crust: Its Composition and Evolution* 312 (Blackwell Scientific Publications, 1985).

102. Pearson, D. G. et al. Re–Os, Sm–Nd, and Rb–Sr isotope evidence for thick Archaean lithospheric mantle beneath the Siberian craton modified by multistage metasomatism. *Geochim. Cosmochim. Acta* **59**, 959–977 (1995).

103. Bevan, D. et al. In situ Rb–Sr dating by collision cell, multicollection inductively-coupled plasma mass-spectrometry with pre-cell mass-filter, (CC-MC-ICPMS/MS). *J. Anal. At. Spectrom.* **36**, 917–931 (2021).

104. Craig, G., Managh, A. J., Stremtan, C., Lloyd, N. S. & Horstwood, M. S. A. Doubling sensitivity in multicollector ICPMS using high-efficiency, rapid response laser ablation technology. *Anal. Chem.* **90**, 11564–11571 (2018).

105. Cheng, P., Koyanagi, G. K. & Bohme, D. K. On the chemical resolution of the ^{87}Rb+(s0)/^{87}Sr+(s1) isobaric interference: a kinetic search for an optimum reagent. *Anal. Chim. Acta* **627**, 148–153 (2008).

106. Hogmalm, K. J., Zack, T., Karlsson, A. K.-O., Sjöqvist, A. S. L. & Garbe-Schönberg, D. In situ Rb–Sr and K–Ca dating by LA-ICP-MS/MS: an evaluation of N_2O and SF_6 as reaction gases. *J. Anal. At. Spectrom.* **32**, 305–313 (2017).

107. Koornneef, J. M., Bouman, C., Schwieters, J. B. & Davies, G. R. Measurement of small ion beams by thermal ionisation mass spectrometry using new 10^{13} Ohm resistors. *Anal. Chim. Acta* **819**, 49–55 (2014).

108. Klaver, M., Smeets, R. J., Koornneef, J. M., Davies, G. R. & Vroon, P. Z. Pb isotope analysis of ng size samples by TIMS equipped with a $10^{13}\,\Omega$ resistor using a ^{207}Pb–^{204}Pb double spike. *J. Anal. At. Spectrom.* **31**, 171–178 (2016).

109. Kimura, J.-I., Chang, Q., Kanazawa, N., Sasaki, S. & Vaglarov, B. S. High-precision in situ analysis of Pb isotopes in glasses using $10^{13}\,\Omega$ resistor high gain amplifiers with ultraviolet femtosecond laser ablation multiple Faraday collector inductively coupled plasma mass spectrometry. *J. Anal. At. Spectrom.* **31**, 790–800 (2016).

110. Vermeesch, P. IsoplotR: a free and open toolbox for geochronology. *Geosci. Front.* **9**, 1479–1493 (2018).

111. Regis, D., Warren, C. J., Mottram, C. M. & Roberts, N. M. Using monazite and zircon petrochronology to constrain the P–T–t evolution of the middle crust in the Bhutan Himalaya. *J. Metamorph. Geol.* **34**, 617–639 (2016).

112. Paton, C., Hellstrom, J., Paul, B., Woodhead, J. & Hergt, J. Iolite: freeware for the visualisation and processing of mass spectrometric data. *J. Anal. At. Spectrom.* **26**, 2508–2518 (2011).

113. Aleinikoff, J. N. et al. Deciphering igneous and metamorphic events in high-grade rocks of the Wilmington Complex, Delaware: morphology, cathodoluminescence and backscattered electron zoning, and SHRIMP U–Pb geochronology of zircon and monazite. *Geol. Soc. Am. Bull.* **118**, 39–64 (2006).

114. Gonçalves, G. O. et al. An assessment of monazite from the Itambé pegmatite district for use as U–Pb isotope reference material for microanalysis and implications for the origin of the "Moacyr" monazite. *Chem. Geol.* **424**, 30–50 (2016).

115. Lamont, T. N. et al. Porphyry copper formation driven by water-fluxed crustal anatexis during flat-slab subduction. *Zenodo* https://doi.org/10.5281/zenodo.13763104 (2024).

116. Sylvester, P. J. Post-collisional alkaline granites. *J. Geol.* **97**, 261–280 (1989).

117. Blatter, D. L., Sisson, T. W. & Hankins, W. B. Crystallization of oxidized, moderately hydrous arc basalt at mid- to lower-crustal pressures: implications for andesite genesis. *Contrib. Mineral. Petrol.* **166**, 861–886 (2013).

118. Ulmer, P., Kaegi, R. & Müntener, O. Experimentally derived intermediate to silica-rich arc magmas by fractional and equilibrium crystallization at 1·0 GPa: an evaluation of phase relationships, compositions, liquid lines of descent and oxygen fugacity. *J. Petrol.* **59**, 11–58 (2018).

119. Yonkee, W. A. & Weil, A. B. Tectonic evolution of the Sevier and Laramide belts within the North American Cordillera orogenic system. *Earth Sci. Rev.* **150**, 531–593 (2015).

Acknowledgements

Author contributions

F.J.C. designed and obtained funding for the project, and T.N.L. led the research. T.N.L., M.A.L. and J.J.W. conceived the idea of crustal-derived magmatism in Arizona, and T.N.L. made the link between flat-slab subduction, water-fluxed crustal anatexis and porphyry copper formation. T.N.L. and A.G. conceived the idea of a geodynamic 'sweet spot'. J.J.W. and M.A.L. pointed out the potential significance of prior Cu enrichment in the Proterozoic lower crust. T.N.L., M.A.L., F.J.C., J.J.W. and A.G. carried out fieldwork in Arizona. T.N.L. compiled the tectonic, geochronological, isotopic and geochemistry compilations. N.M.W.R. carried out U–Th–Pb geochronological analyses, D.B. carried out Rb–Sr geochronological analyses and T.E. oversaw the analyses. T.N.L., N.M.W.R., J.J.W., A.G., A.K., T.E., N.J.G. and S.T. investigated the geochemical and isotopic signatures of the Laramide granites. A.G. provided insights into the Arizona geology and the Laramide Porphyry Province. T.N.L. carried out petrological investigations, EPMA analyses and petrological modelling. T.N.L. wrote the first draft of the manuscript. All authors contributed to subsequent drafts.

Competing interests

The authors declare no competing interests.

Additional information

Extended data is available for this paper at https://doi.org/10.1038/s41561-024-01575-2.

Supplementary information The online version contains supplementary material available at https://doi.org/10.1038/s41561-024-01575-2.

Correspondence and requests for materials should be addressed to Thomas N. Lamont.

Peer review information *Nature Geoscience* thanks Joshua Schwartz and Richard Sillitoe for their contribution to the peer review of this work. Primary Handling Editor: Alison Hunt, in collaboration with the *Nature Geoscience* team.

**Reprints and permissions information** is available at www.nature.com/reprints.
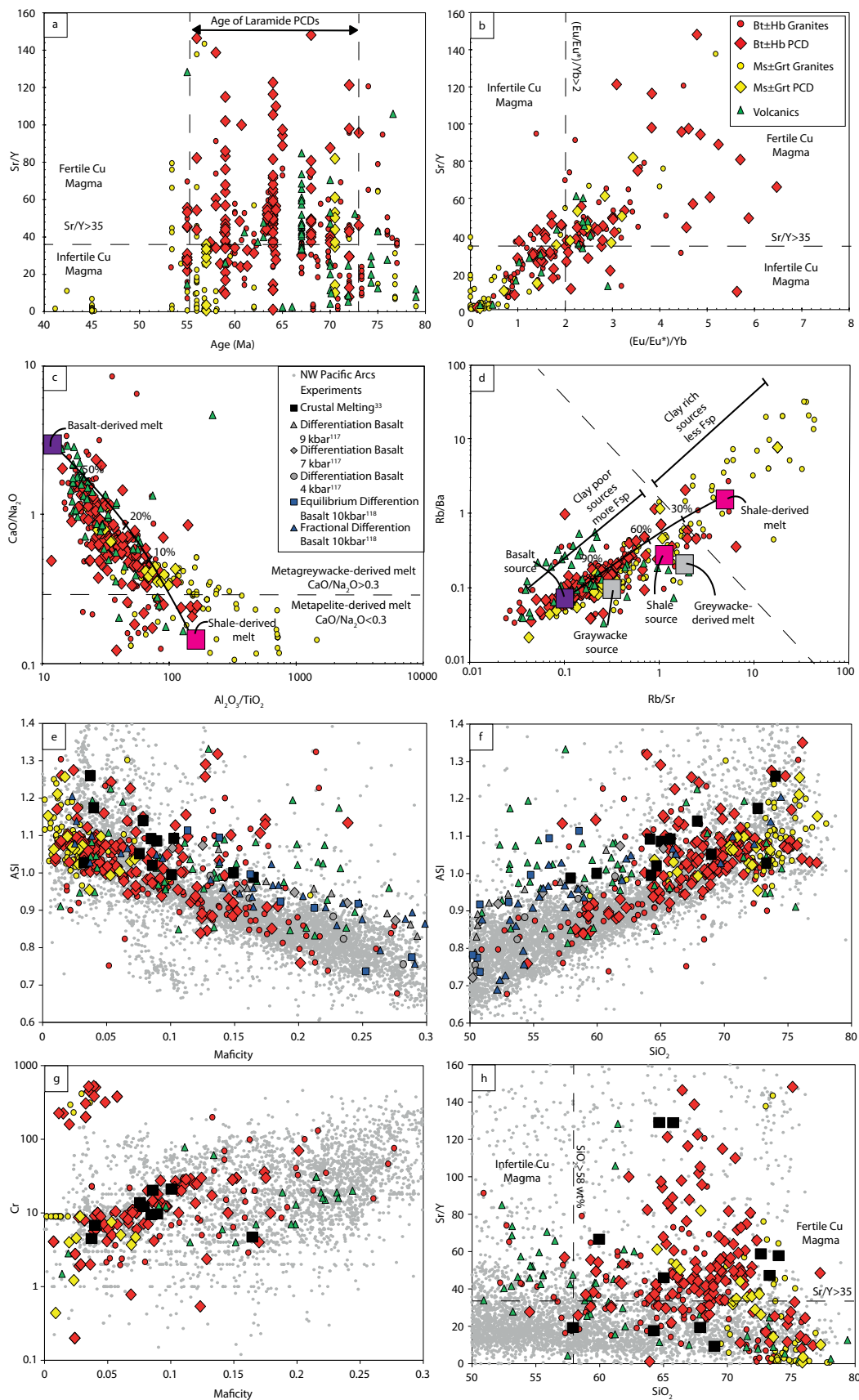
Extended Data Fig. 1 | See next page for caption.

Extended Data Fig. 1 | Whole rock geochemical plots showing key features of Laramide granites in Arizona. a) Sr/Y vs age (Ma) and **b**) Sr/Y vs (Eu/Eu*)/Yb for Laramide volcanic rocks, biotite ± hornblende-bearing and muscovite ± garnet-bearing granites. Sr/Y > 35 and (Eu/Eu*)/Yb>2 indicate fertile porphyry magma[15]. **c**) CaO/Na$_2$O-Al$_2$O$_3$/TiO$_2$ plot and **d**) Rb/Ba–Rb/Sr plot[116], both showing melting output of a basalt and sediment derived melt, with biotite ± hornblende-bearing granites overlapping with the basalt derived melt and the muscovite ± garnet-bearing granites overlapping with the sediment derived melt. **e-h**) Geochemical plots of the Laramide granites with NW Pacific arc rock compilation and experimental data[33,117,118], showing the Laramide intrusions overlap with the compositions of crustal-derived melts[33]. The full suite of whole-rock geochemical data is presented in Supplementary Table 2.
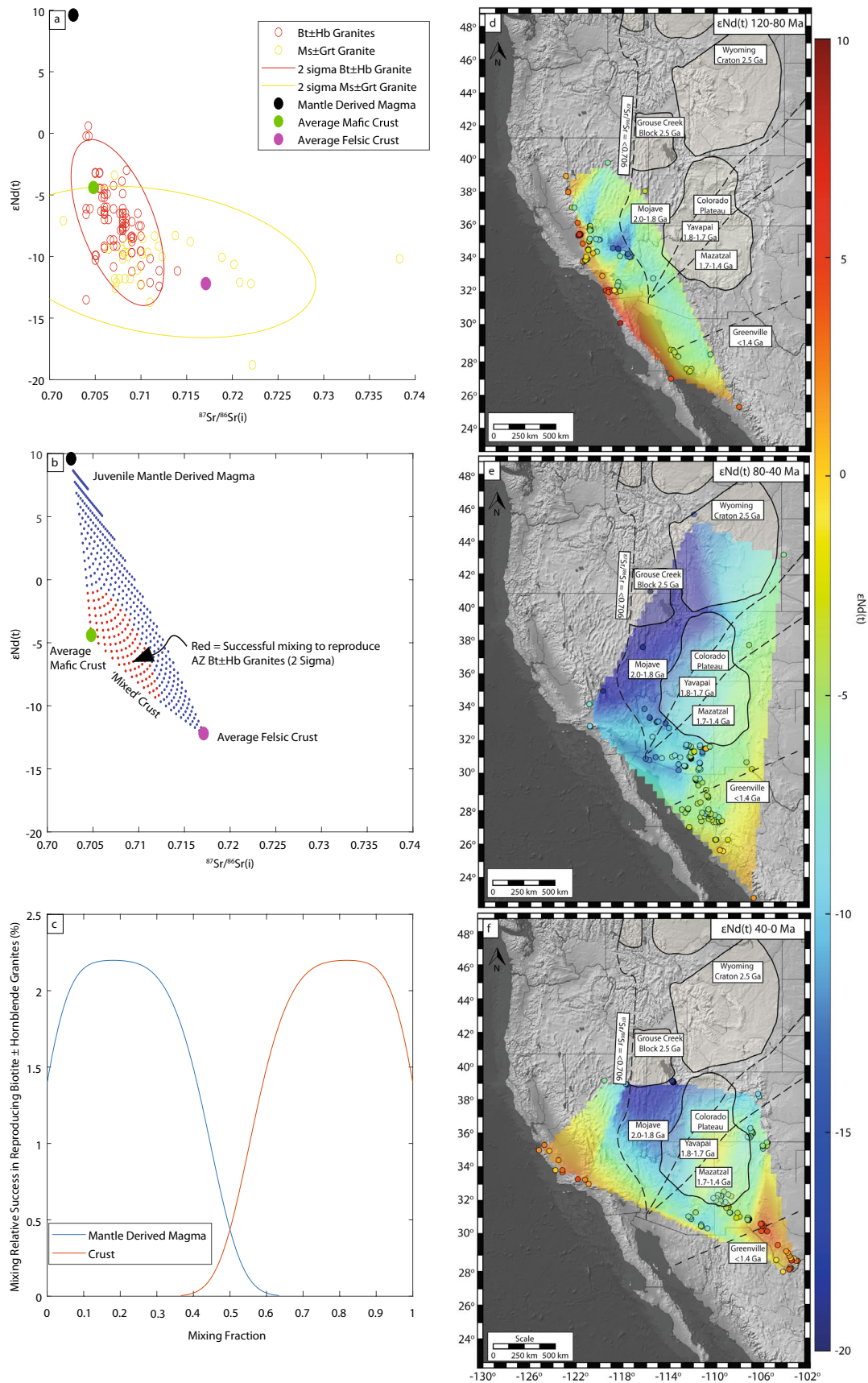
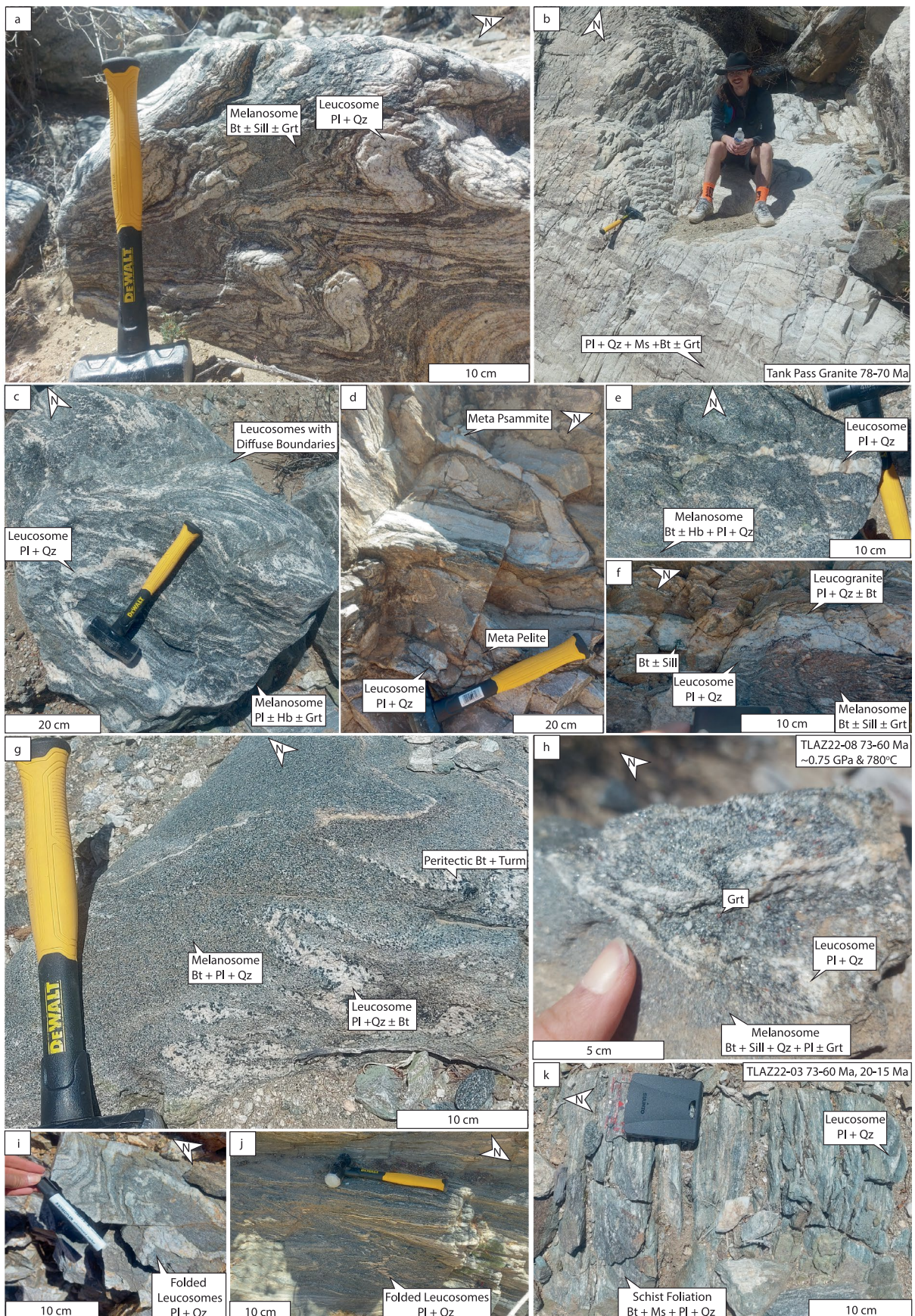**Extended Data Fig. 2 | See next page for caption.**

Extended Data Fig. 2 | Isotopic mixing calculations and spatial and temporal Nd isotope evolution maps of the SW USA and NW Mexico. a-c) Sr–Nd isotope mixing calculations between average felsic Proterozoic crust, mafic Proterozoic crust and juvenile mantle, with relative success rate (%) plots of mixing calculations to produce the correct composition of the observed Laramide biotite ± hornblende-bearing granites (see Supplementary Material for full details). **d-f)** εNd(*t*) compilation maps of granitic rocks from the SW USA and NW Mexico binned by the intrusion U–Pb age and colour coded for εNd(t) value. **d**) 120–80 Ma, **e**) 80–40 Ma, **f**) 40–0 Ma. Locations of cratons and Proterozoic terrane boundaries derived from sources[17,26,47].
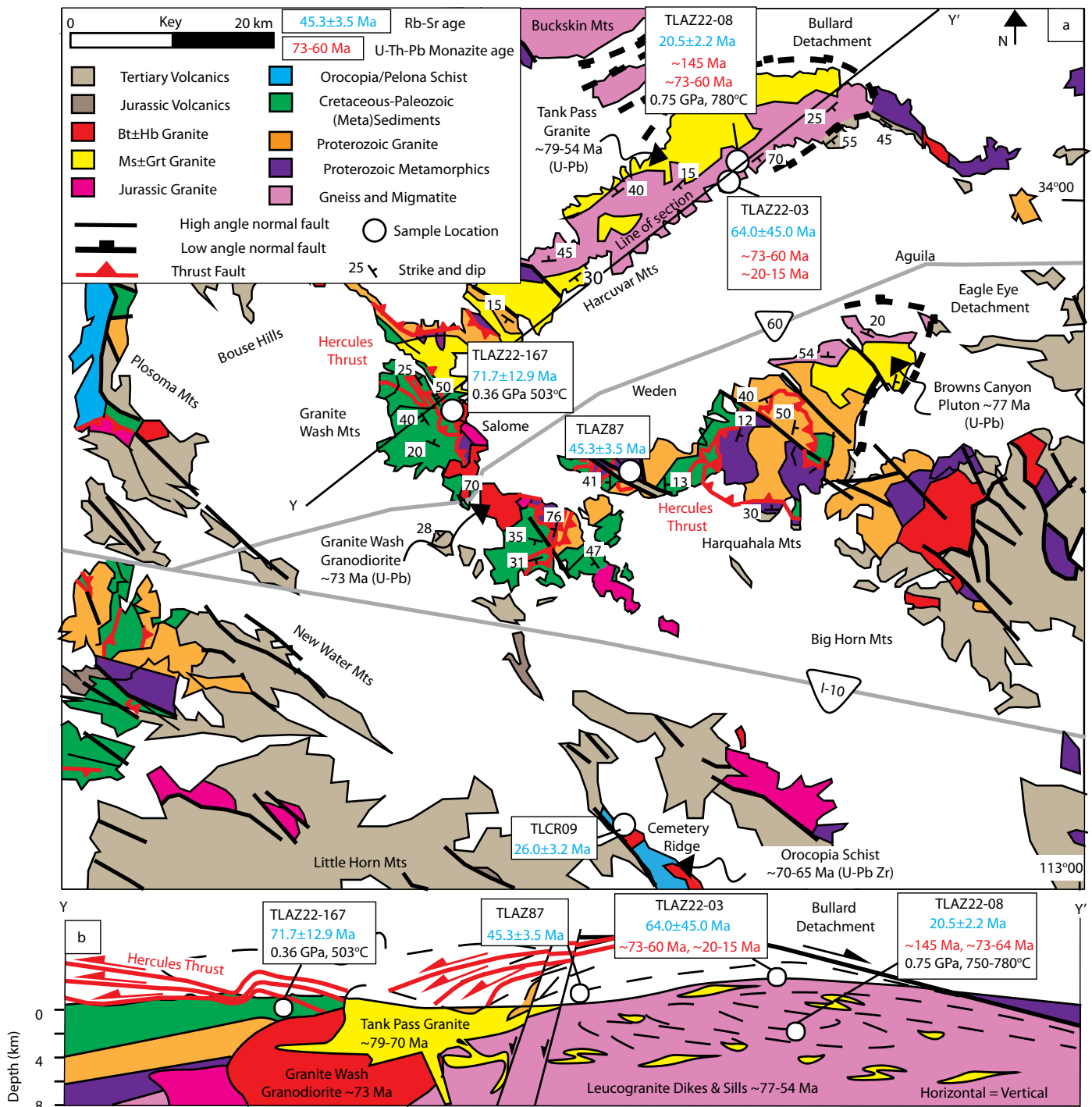
Extended Data Fig. 3 | Summary Geological Maps of Harcuvar, Harquahala and Granite Wash Mountains and cross-sections showing sample locations. **a)** Study area map and sample locations in the Harcuvar, Harquahala and Granite Wash Mountains metamorphic core complexes and exposures of the Farallon Plate at Cemetery Ridge. Data from ref. 58. **b)** Schematic cross section through the Harcuvar and Granite Wash Mountains showing the key structural

relationships of: i) the Hercules Thrust being folded and cross-cut by the ~73 Ma Granite Wash Granodiorite and ~78–70 Ma Tank Pass Granite, ii) metamorphic grade increasing with increasing structural depth beneath the Hercules Thrust and iii) the extensional Bullard detachment cross-cutting the older compressional features.

Extended Data Fig. 4 | See next page for caption.

Extended Data Fig. 4 | Outcrop photographs of migmatites and melting textures from the Harcuvar Mountains. Outcrop photographs of migmatites and melting textures from the Harcuvar Mountains (GPS: 34.056997, -113.314824), showing plagioclase rich (trondhjemitic) leucosomes with diffuse boundaries in textural equilibrium with garnet, sillimanite and biotite-bearing melanosomes. Melt domains are locally extensive (>35% estimated rock volume) and pytgmatically folded and connect to form larger leucogranite bodies (for example Tank Pass pluton) exposed at higher structural levels.
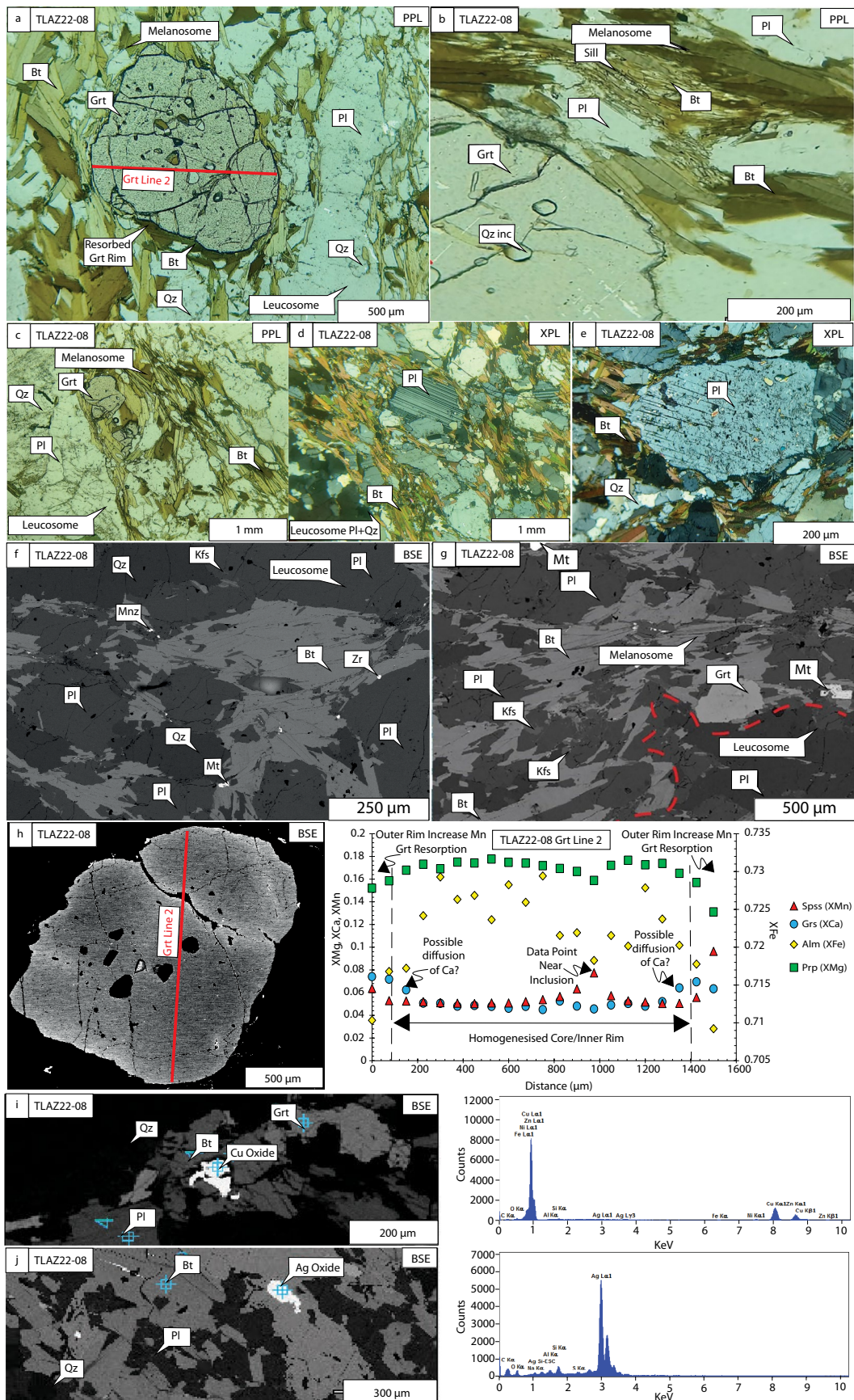
Extended Data Fig. 5 | See next page for caption.

Extended Data Fig. 5 | Summary of petrographic and textural features in Harcuvar Mountains Migmatites. Plane polarized light (PPL), and cross polarized light (XPL) photomicrographs and backscattered electron (BSE) images of Harcuvar Mountains migmatites (TLAZ22-08). **a**) PPL image of garnet and biotite bearing melanosome adjacent to leucosome (plagioclase and quartz rich domain). **b**) High resolution PPL image of garnet with straight facies in equilibrium with prismatic sillimanite, plagioclase, quartz and minimal peritectic k-feldspar. **c**) PPL image of a pytgmatically folded leucosome and melanosome. **d-e**) XPL photomicrographs of coarse plagioclase rich leucosomes rimmed by biotite rich melanosomes. **f-g**) BSE images of leucosome and melanosomes showing the minimal amount of K-feldspar in textural equilibrium with garnet, plagioclase, biotite, sillimanite, quartz, magnetite. **h** and **i**) A garnet chemical traverse showing endmember molar proportions of pyrope (XMg) grossular (XCa), spessartine (XMn), and almandine (XFe). Profiles show flat homogenized cores with increasing spessartine content towards the outer rim indicative of garnet resorption, note grossular also increases at the inner rim potentially due to diffusion associated with garnet resorption. **j** and **k**) BSE images and electron dispersive spectra of Cu and Ag oxides. Full electron probe microanalysis Data in Supplementary Table 4.
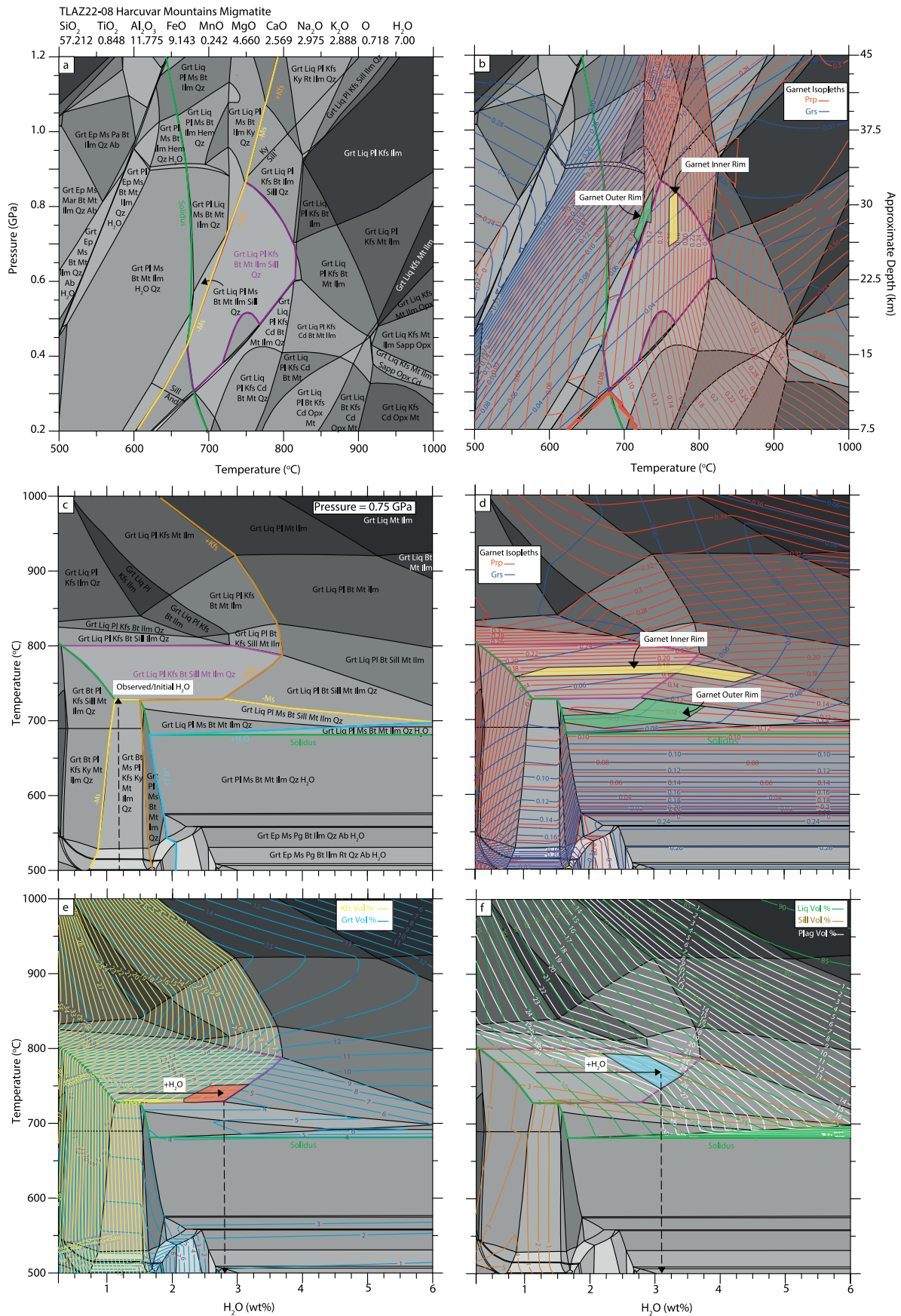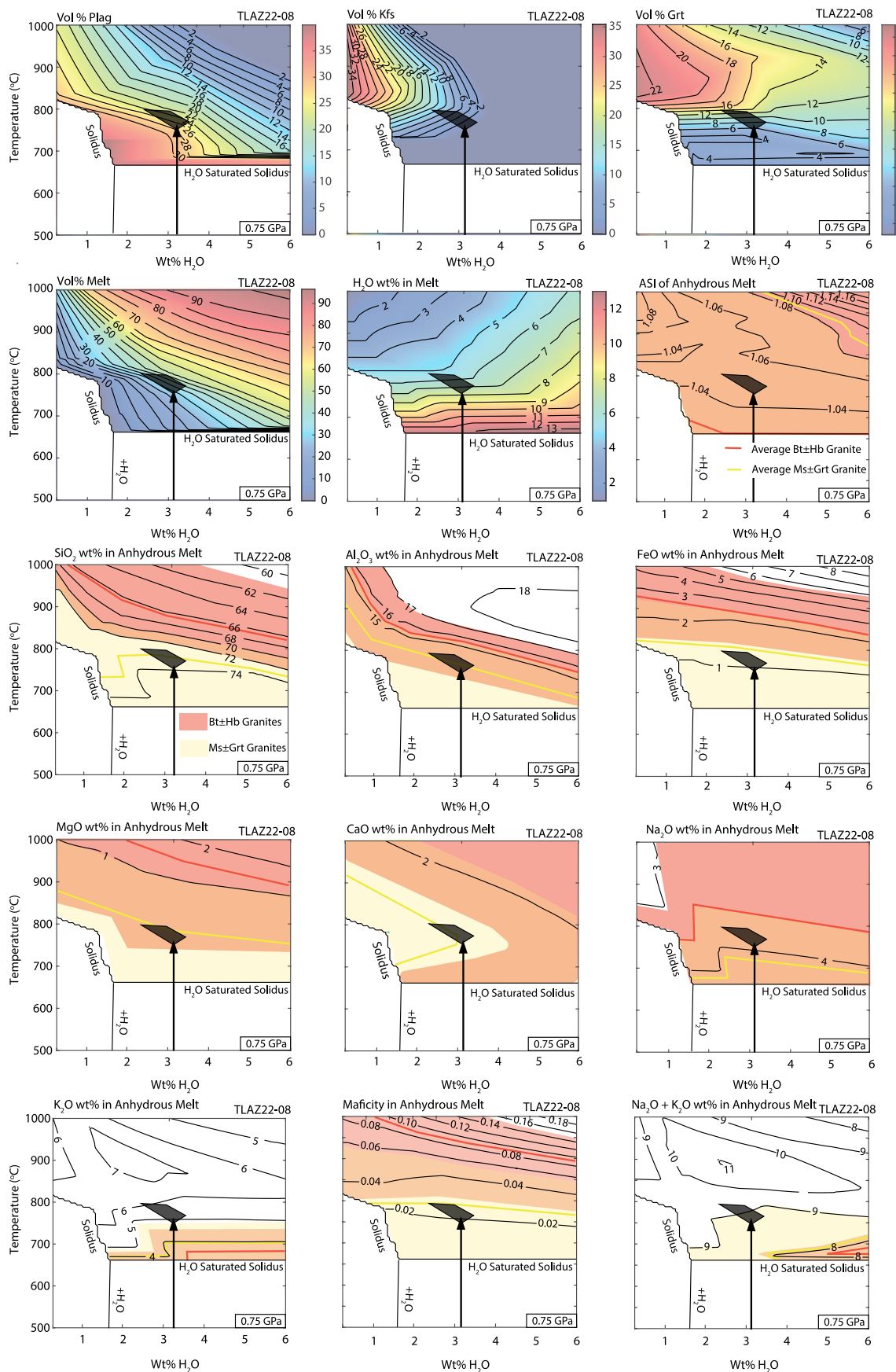
Extended Data Fig. 6 | See next page for caption.

Extended Data Fig. 6 | Petrological modelling results for Harcuvar Mountains migmatite sample TLAZ22-08. Equilibrium phase diagrams for sample TLAZ22-08 showing predicted assemblage fields and phase isopleths intersections in pressure–temperature–X(H_2O) space. **a**) Phase diagram in pressure–temperature space with 7% mole H_2O, showing phase boundaries and reaction topologies with all free water being consumed upon crossing the water saturated solidus. Observed peak assemblage in red text. **b**) Garnet isopleth compositions for pyrope and grossular, with polygons that overlay intersections that correspond to garnet core and outer rim. **c**) Isobaric Temperature–X(H_2O) phase diagram at 0.75 GPa, varying bulk-rock H_2O content from 0.25 wt% to 6 wt% with observed assemblage field in red text. **d**) Garnet pyrope and grossular compositional isopleths with polygons representing observed garnet core and outer rim compositions. **e**) K-feldspar and garnet volume isopleths with polygons showing intersections at observed volume proportions. **f**) Melt volume, plagioclase and sillimanite volume isopleths, with polygons showing the observed phase proportions and leucosome proportions.

Extended Data Fig. 7 | See next page for caption.

Extended Data Fig. 7 | Predicted melt compositions for variable Temperature-$X(H_2O)$ water-fluxed batch melting scenarios for Harcuvar Mountains migmatite sample TLAZ22-08. Petrological modelling outputs showing predicted melt volume, water content (wt%) in the melt and volume proportions of k-feldspar, plagioclase and garnet, with major element composition (wt%). Calculations were performed isobaric at a pressure of 0.75 GPa, varying temperature and $X(H_2O)$ (0.25–6 wt% H_2O). Red and yellow lines mark average biotite ± hornblende and muscovite ± garnet-bearing granites, and red and yellow fields mark the observed range in biotite ± hornblende and muscovite ± garnet-bearing granites respectively. All geochemical data of Laramide granites is available in Supplementary Table 2.
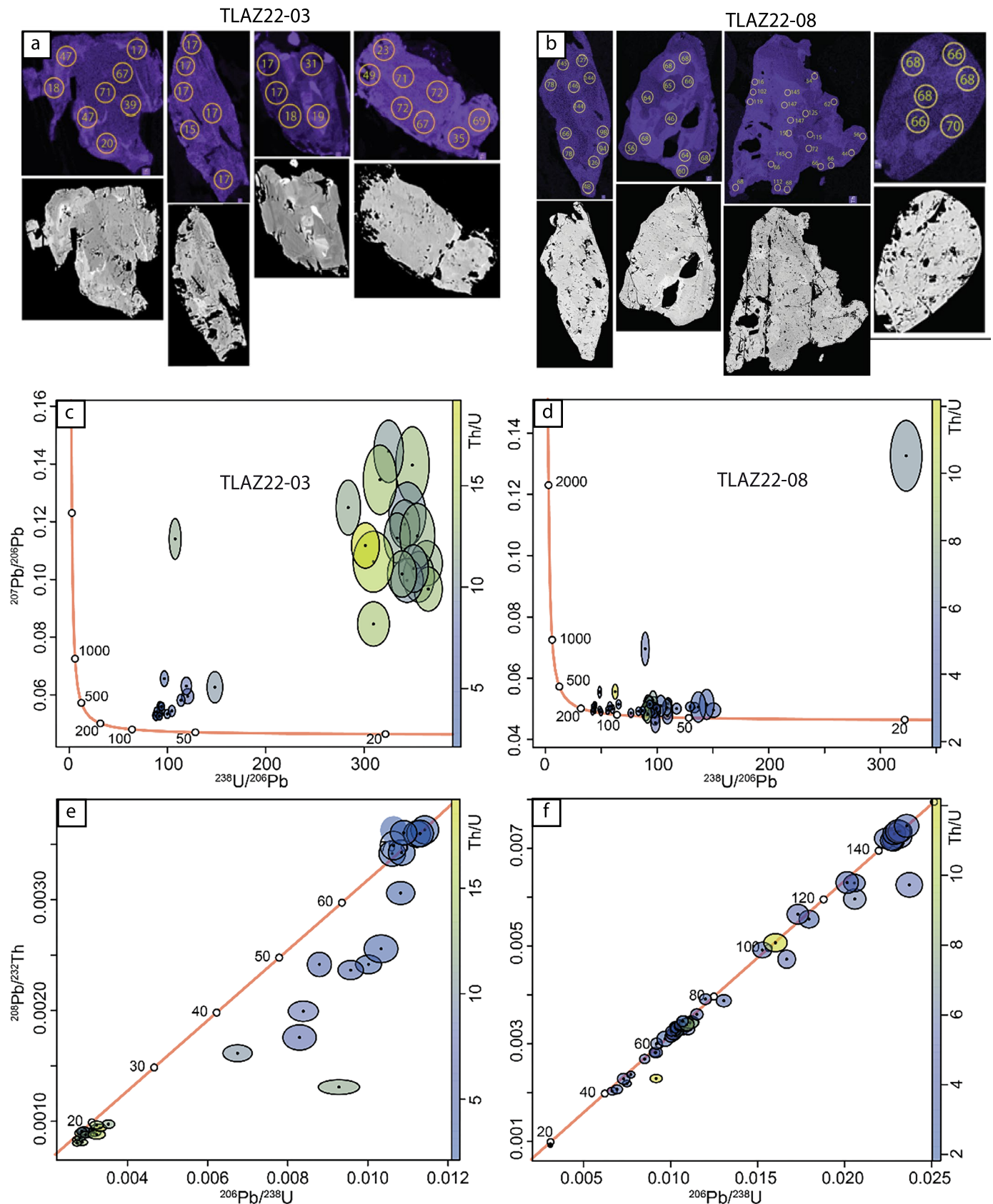
Extended Data Fig. 8 | Summary of monazite U–Th–Pb geochronological data from Harcuvar Mountains samples TLAZ22-08 and TLAZ22-03. a-b) Example monazite chemical maps showing the locations where laser analysis was performed, c-d) Tera-wasserburg of all monazite U–Th–Pb data before common lead correction (colour coded for Th/U). e-f) $^{206}Pb/^{238}U$ vs. $^{208}Pb/^{232}Th$ plots using common lead corrected U–Th–Pb data (colour coded for Th/U). Full U–Th–Pb data is in Supplementary Table 7.
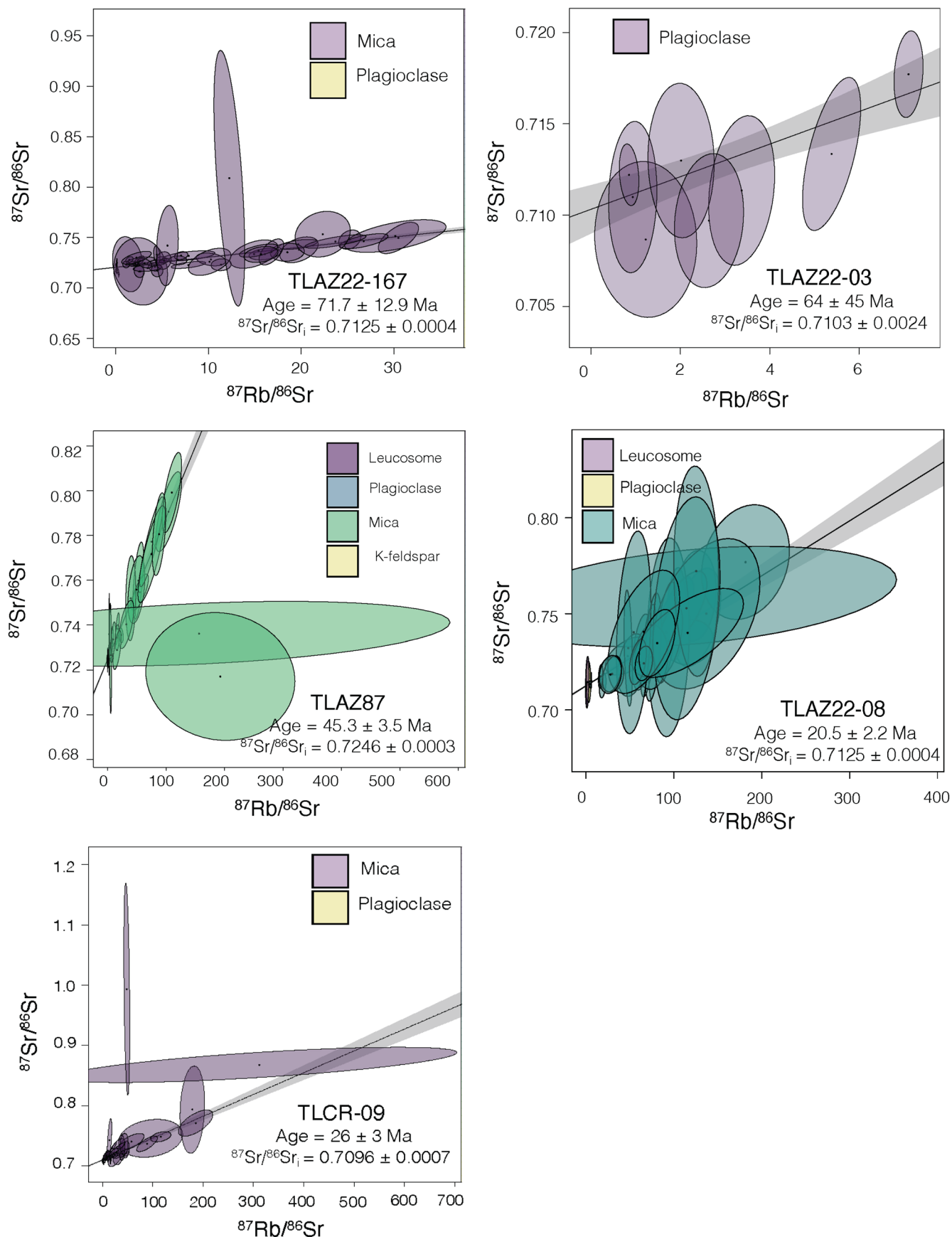
Extended Data Fig. 9 | In-situ Rb–Sr isochron plots. In-situ Rb–Sr isochron plots for mica, plagioclase and k-feldspar from samples TLAZ22-167, TLA22-03, TLAZ22-08, TLAZ87 and TL-CR-09. Full Results in Supplementary Table 6.
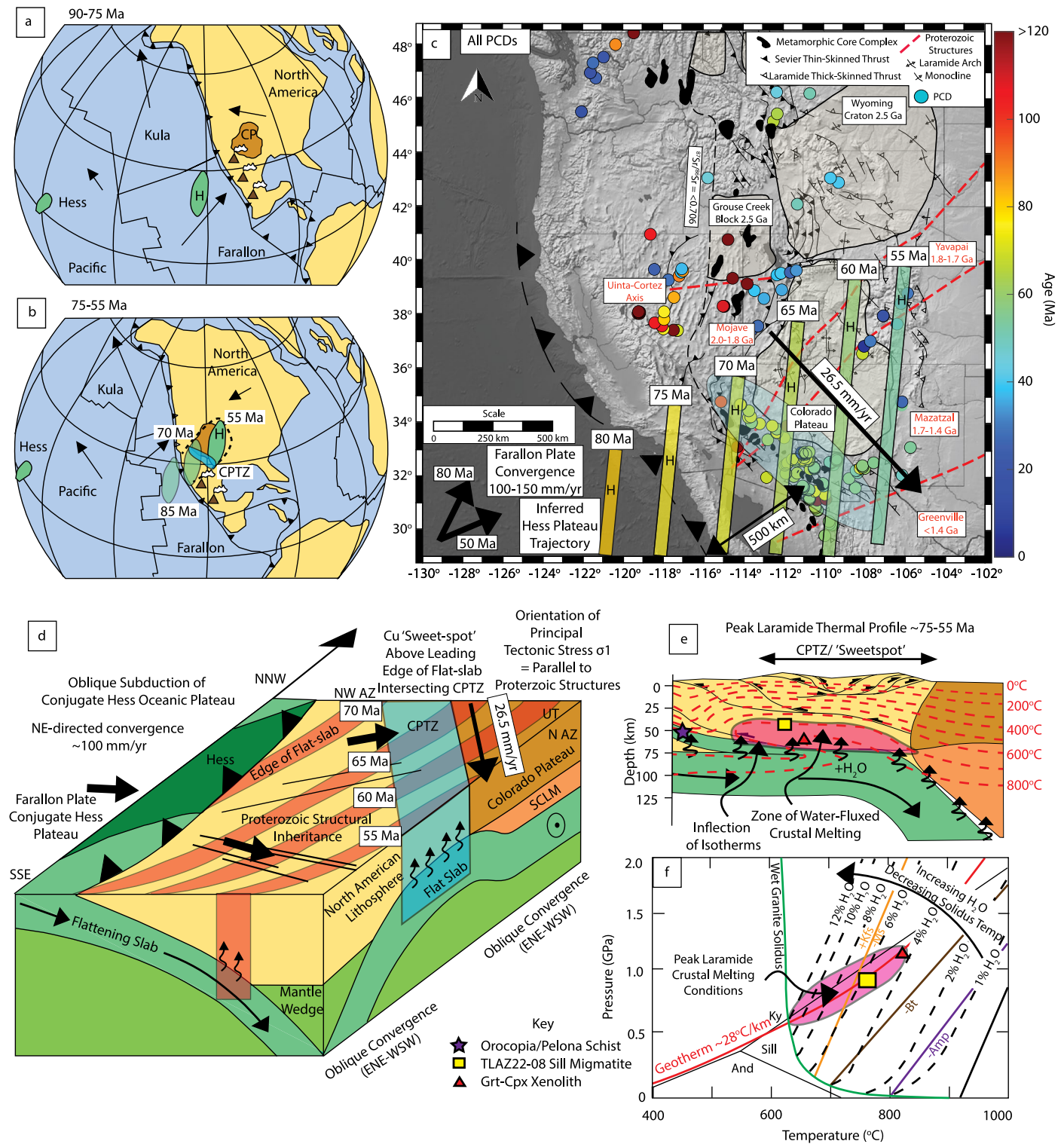
Extended Data Fig. 10 | Summary geodynamic model for Hess plateau subduction and diachronous onset of slab flattening leading to water fluxed crustal anatexis. a-b) Global plate reconstructions of the Hess conjugate showing the oblique intersection with the trench at ~75–70 Ma causing diachronous slab-flattening towards the SE. Data from refs. 20,21,119. **c)** Map of Western USA with sequential 'sweet-spot' advance related to slab geometry. Data from refs. 3,17,23,26,47,51,52. **d)** Cartoon block model showing the geometric relationship of the Cu 'sweetspot' on the leading edge of the flat-slab relative to

the conjugate Hess subduction. **e)** Schematic crustal temperature distribution for a 2-D flat-slab at the hypothesized 'sweetspot' based on the new pressure-temperature data and Orocopia Schist data[49–51]; note the inverted isotherms on the trench-ward side of the 'sweetspot' due to continued underthrusting of a flat-slab causing cooling of the upper-plate. **f)** Schematic pressure-temperature phase diagram showing the decrease in granitic solidus with increasing addition of water. Data from ref. 61.